

## LOCAL VARIATIONS OF THE RADIAL METALLICITY GRADIENT IN A SIMULATED NIHAO-UHD MILKY WAY ANALOGUE AND THEIR IMPLICATIONS FOR (EXTRA-)GALACTIC STUDIES

SVEN BUDER<sup>1,2,\*</sup>, TOBIAS BUCK<sup>3,4</sup>, QIAN-HUI CHEN (陈千惠)<sup>1,2</sup>, AND KATHRYN GRASHA<sup>1,2,\*</sup>

<sup>1</sup>Research School of Astronomy and Astrophysics, Australian National University, Canberra, ACT 2611, Australia

<sup>2</sup>ARC Centre of Excellence for All Sky Astrophysics in 3 Dimensions (ASTRO 3D), Australia

<sup>3</sup>Universität Heidelberg, Interdisziplinäres Zentrum für Wissenschaftliches Rechnen, Im Neuenheimer Feld 205, D-69120 Heidelberg, Germany and

<sup>4</sup>Universität Heidelberg, Zentrum für Astronomie, Institut für Theoretische Astrophysik, Albert-Ueberle-Strae 2, D-69120 Heidelberg, Germany

Version April 4, 2025

### ABSTRACT

Radial metallicity gradients are fundamental to understanding galaxy formation and evolution. In our high-resolution simulation of a NIHAO-UHD Milky Way analogue, we analyze the linearity, scatter, spatial coherence, and age-related variations of metallicity gradients using young stars and gas. While a global linear model generally captures the gradient, it overestimates metallicity in the inner galaxy and underestimates it in the outer regions of our simulated galaxy. Both a quadratic model, showing an initially steeper gradient that smoothly flattens outward, and a piecewise linear model with a break radius **around 9.3-11.5 kpc (2.4-3.0 effective radii)** fit the data equally well. The spread of [Fe/H] of young stars in the simulation increases by tenfold from the innermost to the outer galaxy at a radius of 20 kpc. We find that stars born at similar times along radial spirals drive this spread in the outer galaxy, with a chemical under- and over-enhancement of up to 0.1 dex at leading and trailing regions of such spirals, respectively. This localised chemical variance highlights the need to examine radial and azimuthal selection effects for both Galactic and extragalactic observational studies. The arguably idealised but volume-complete simulations suggest that future studies should not only test linear and piecewise linear gradients, but also non-linear functions such as quadratic ones to test for a smooth gradient rather than one with a break radius. Either finding would help to determine the importance of different enrichment or mixing pathways and thus our understanding of galaxy formation and evolution scenarios.

*Subject headings:* Galaxy: structure – Galaxy: abundances – galaxies: structure – galaxies: abundances

### 1. INTRODUCTION

Understanding the radial metallicity gradient, defined as the change in heavy element abundance with galactocentric radius, in galaxies provides critical insights into their formation and evolutionary processes, such as inside-out formation, gas accretion, outflows, and radial migration (e.g. Quirk & Tinsley 1973; Tinsley 1980; Lacey & Fall 1985; Wyse & Silk 1989; Kauffmann 1996; Chiappini et al. 1997; Schönrich & Binney 2009; Moran et al. 2012; Bird et al. 2013). The decrease in metallicity with increasing distance from the Galactic centre is well-established both theoretically (Larson 1976; Tinsley 1980; Chiosi 1980) and observationally in the Milky Way (Searle 1971; Janes 1979; Twarog et al. 1997) and other massive spiral galaxies (e.g. Tinsley 1980; Zaritsky et al. 1994; Bresolin et al. 2012). The Milky Way, being the only galaxy where we can resolve millions of stars, provides a unique opportunity to study these gradients and deviations from them in detail. Early evidence by Janes (1979) suggested a linear gradient on the order of  $d[\text{Fe}/\text{H}]/dR = -0.05 \pm 0.01 \text{ dex kpc}^{-1}$  for the Milky Way which aligns very well with more recent measurements (Anders et al. 2017; Hayden et al. 2015). However, these gradients are accompanied by a significant spread in [Fe/H] of 0.1 – 0.15 dex, as noted by Twarog (1980), which may imply a fine structure of the metallicity gradient (see Genovali et al. 2014).

With increasing sample size and measurement precision, the specific shape and characteristics of this gradient remain somewhat unclear (Chiappini 2002). Previous studies have

for example claimed more intricate non-linear trends, bends, and flattening in the gradient of the Milky Way (e.g. Donor et al. 2020) and other galaxies (e.g. Pilyugin 2003; Sánchez et al. 2014) or even sequences of shapes (Pilyugin et al. 2017; Pilyugin & Tautvaišienė 2024), which were fitted with different models (Rosales-Ortega et al. 2011; Bresolin et al. 2012), such as piecewise linear ones (e.g. Sánchez-Menguiano et al. 2016) or non-linear ones (e.g. Scarano & Lépine 2013).

Variations in the metal distribution, including breaks of the gradient at specific radii, give rise to a plethora of possible physical explanations, such as star formation efficiency variations and localised star formation bursts (Sánchez et al. 2014; Sánchez-Blázquez et al. 2014; Ho et al. 2015), gas accretion and dilution at different rates (Bresolin et al. 2012; Sánchez et al. 2013; Belfiore et al. 2016; Sánchez-Menguiano et al. 2016), gas outflows and feedback (Lilly et al. 2013; Ma et al. 2017a), as well as disk instabilities or local overdensities (Grand et al. 2016; Ho et al. 2017). In particular, Scarano & Lépine (2013) suggested that gradient break radii coincided with the corotation radii of spiral arms.

Recent advancements in both computations and observations have significantly expanded our capabilities. For example, in terms of observational data in the Milky Way, the *Gaia* mission (Gaia Collaboration et al. 2016) enables more detailed studies of these gradients. New suites of large-scale simulations now allow us to gain insights into radial metallicity gradients across a range of simulated galaxies, including Milky Way analogues. This presents opportunities to revisit outstanding challenges of the detailed shape of the radial metallicity gradient. For instance, Hogg et al. (2019) created an extensive metallicity map of the Milky Way using APOGEE and *Gaia*

E-mail: sven.buder@anu.edu.au

\*Australian Research Council DECRA Fellow

data, while Poggio et al. (2022) mapped young stars and found metallicity variations around spiral arms (see also Zari et al. 2018, 2021; Poggio et al. 2021; Hackshaw et al. 2024). Similarly, Imig et al. (2023, among others) traced gradients across different stellar populations and ages, emphasizing the importance of considering radial migration effects (Binney & Tremaine 2008; Frankel et al. 2018, 2020).

Historically, radial metallicity gradients have been measured using various stellar populations and gas tracers. Estimated gradients seem to be broadly consistent across different stellar tracers, such as young open clusters (e.g. Yong et al. 2012; Cunha et al. 2016; Magrini et al. 2017; Casamiquela et al. 2019; Donor et al. 2020; Spina et al. 2021; Myers et al. 2022), young hot (OB-type) stars (Zari et al. 2018, 2021; Poggio et al. 2021, 2022), field stars close to the Galactic plane (e.g. Bergemann et al. 2014) or Cepheids (Andrievsky et al. 2002a,b; Lemasle et al. 2007, 2013).

Despite extensive observational efforts, several challenges persist for studies in the Milky Way. The completeness (or patchiness) of observed datasets remains a fundamental issue (Bergemann et al. 2014). The robustness of fits to the incomplete data is still contentious, including the need to actually fit two linear gradients with a break radius at corotation radius (Bresolin et al. 2012, and references therein) or further out (Yong et al. 2012; Donor et al. 2020) - or even more complicated functions (see e.g. Chiappini et al. 2001; Kubryk et al. 2015). Furthermore, methodologies for fitting linear models to scattered data need re-evaluation (Metha et al. 2021). Different samples yield varying gradients, potentially due to biases in data or the inclusion of older stars (e.g. Allende Prieto et al. 2006; Hayden et al. 2014; Anders et al. 2014; Vickers et al. 2021; Willett et al. 2023). The impact of spiral arm structures (Poggio et al. 2021), the Galactic warp (Lemasle et al. 2022) or bar-driven mixing (Di Matteo et al. 2013) on metallicity gradients is not fully understood.

Understanding these gradients in the Milky Way is also crucial for extragalactic studies, where spatial resolution limits observations in different ways. In extragalactic systems, metals are mainly traced via gas, because it provides a more direct measure of the ongoing enrichment processes, unlike stars, which primarily reflect the integrated chemical history of the past. Observationally, gas emission lines are typically brighter and more accessible across large distances than stellar absorption lines, allowing for broader spatial coverage, especially in distant galaxies. Consequently, extragalactic studies often focus on gas-phase metallicity as traced by oxygen,  $A(O) = 12 + \log(O/H)$ , while Galactic studies typically use stellar iron abundance  $[Fe/H] = A(Fe) - A(Fe)_\odot$  as a metallicity tracer (e.g. Nicholls et al. 2017; Fraser-McKelvie et al. 2022).

New instruments like the MUSE integral field spectrograph have enabled a plethora of extragalactic studies to contrast the Milky Way and techniques like the spectroscopy of H II regions and planetary nebulae have helped to infer gas metallicity distributions in external galaxies (Shaver et al. 1983; Vilchez & Esteban 1996; Rolleston et al. 2000; Bresolin et al. 2012). Recent examples include Sánchez et al. (2014) with CALIFA galaxy observations as well as Mun et al. (2024) and Chen et al. (2024a) who use MAGPI observations to probe for example the effects of spiral arms. Notable is also the scatter that Chen et al. (2023) found for the gas metallicity across galactic radii with TYPHOON observations (see their Figs. 4-6). Grasha et al. (2022) found that the gas metallicity gradient plateaus at a lower limit in their TYPHOON galaxies at the outermost

radii - an observation replicated by IllustrisTNG simulations (Hemler et al. 2021; Garcia et al. 2023).

From a modelling perspective, galactic chemical evolution models can both test understanding of radial metallicity gradients and make predictions beyond the limited volumes and tracers tested by Milky Way and extragalactic studies. Such galactic chemical evolution models include Chiappini et al. (2001); Matteucci & Recchi (2001); Minchev et al. (2014); Kubryk et al. (2015); Stanghellini et al. (2015); Rybizki et al. (2017); Spitoni et al. (2023); Johnson et al. (2024). Sharda et al. (2021) even presented a model for gas phase metallicity gradients in galaxies and their evolution from first principles (see also Krumholz & Ting 2018).

In exploring radial metallicity gradients through simulations, we have better understood how different processes influence these gradients across galactic models and temporal scales. Studies such as Pilkington et al. (2012) in RaDES simulations reveal that gradients are typically established via inside-out galaxy formation. Khoperskov et al. (2023) quantified the scatter of gas metallicity to  $\approx 0.04 - 0.06$  dex at a given galactocentric distance in their simulations. Meanwhile, the EAGLE simulations used by Tissera et al. (2019) provide insights into how these gradients vary with galaxy characteristics like stellar mass and merger history, emphasizing the dynamic nature of metallicity distributions. The plethora of simulations such as AURIGA (Grand et al. 2016), FIRE (Ma et al. 2017b, see their Fig. 6) or VINTERGATAN (see their Fig. 9; Agertz et al. 2021) also allow us to explore the gradient evolution of galactic timescales. Buck et al. (2023), for example, found a link of major accretion events with periods of unexpected steepening in the metallicity gradient within NIHAO-UHD simulations – closely resembling findings for the Milky Way by Lu et al. (2022) and Ratcliffe et al. (2023). FIRE simulations, examined by Bellardini et al. (2021), Bellardini et al. (2022), Orr et al. (2023), and Graf et al. (2024), extend these findings by comparing radial metallicity gradients and their azimuthal scatter across gas and stellar components and illustrate the complex interplay between galactic structure and metal enrichment processes. Similarly, Grand et al. (2015, 2016) highlight temporal changes in metallicity gradients already within 120 Myr, or roughly one galactic rotation. Such rapid changes underscore the impact of transient galactic events on the metal distribution, linking them to star formation patterns along spiral arms and the broader evolutionary history of the galaxy.

In this study, we analyze a high-resolution NIHAO-UHD simulation of a Milky Way analogue to bridge the observational gap between detailed studies of our galaxy and broader extragalactic surveys. We aim to reveal subtle features of the radial metallicity gradient, which may be obscured by observational constraints in both the Milky Way and distant galaxies, by testing the following properties within the observationally probed inner  $R_{\text{Gal}} \leq 20$  kpc:

1. *Linearity of the gradient:* Assess the extent to which the radial metallicity gradient of young stars is linear.
2. *Scatter in the gradient:* Quantify the expected scatter in the radial metallicity gradient of young stars.
3. *Coherence of the gradient with position:* Investigate the gradient's variation with radial coverage and azimuth.
4. *Coherence of the gradient with age:* Test the reliability of stars as tracers of the gas disk over different ages.

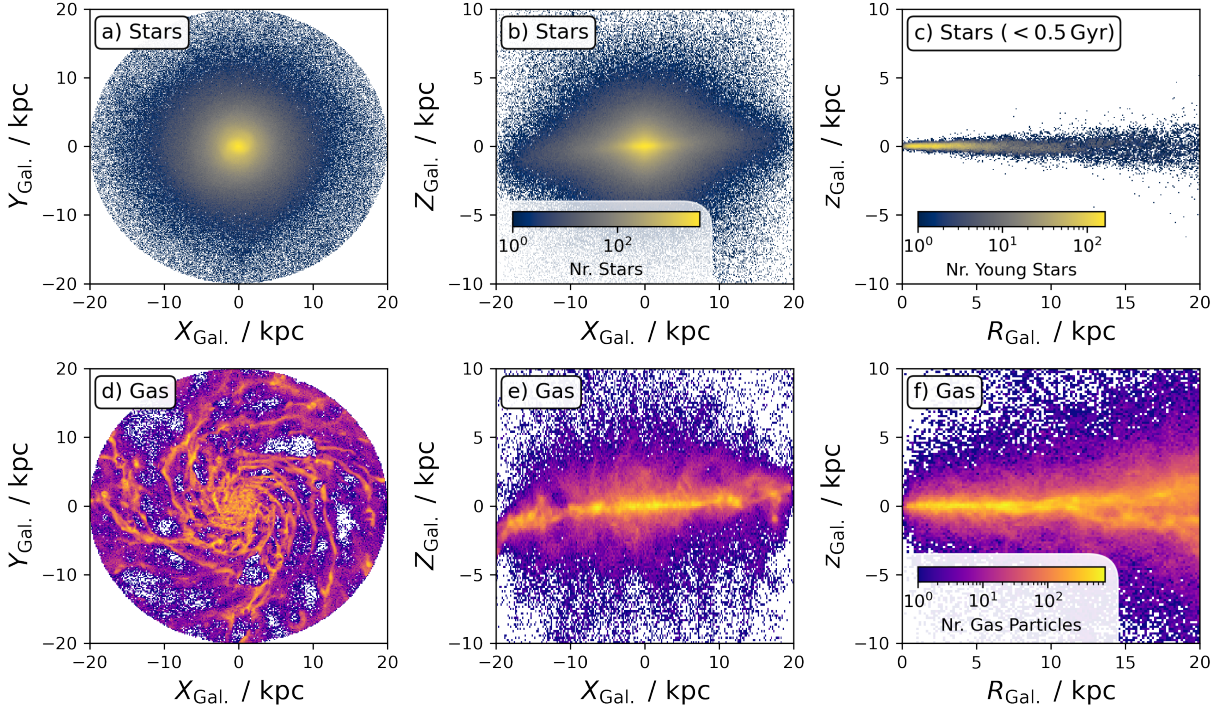


FIG. 1.— Logarithmic spatial density distribution of stars (upper panels) and gas (lower panels) within  $R < 20$  kpc  $\sim 5 R_e$  of the NIHAO-UHD Milky Way analogue g8.26e11 in galactocentric cartesian and cylindrical coordinates. Panel c) shows the influence of selecting only stars with ages below 0.5 Gyr.

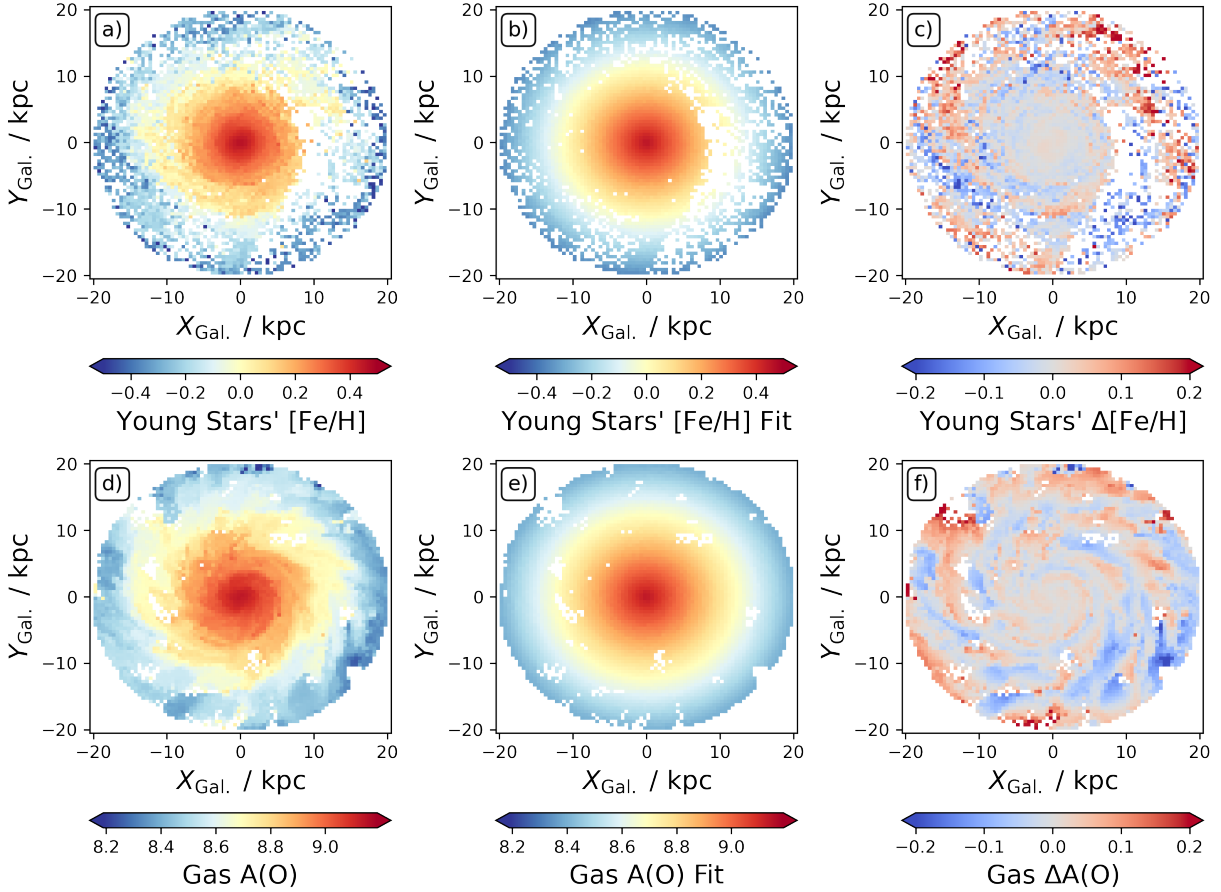


FIG. 2.— Face-on view of average simulated metallicity (left panels), a linear radial fit to it (middle panels, see Section 3.1 and Eq. 1) and the fit residuals (right panels) in bins of 0.5 kpc. Shown are metallicity as traced by young star iron abundances (top panels) and gas phase metallicity (bottom) panels.

The paper is structured as follows: Section 2 describes the data of our Milky Way analogue NIHAO-UHD simulation. Section 3 analyses the linearity of the radial metallicity gradient of the simulation, the first of our four objectives. Section 4 then analyses both the scatter and local deviations from the gradient as well as the coherence of the gradient with vertical and azimuthal position as well as age (the remaining three objectives). Section 5 discusses them individually. We note that in this research we are mainly interested in the specific shape of the radial metallicity gradient for radii relevant to Galactic observations. However, we also discuss our results in the context of extragalactic results that probe beyond the inner 20 kpc of a galaxy. Section 6 bundles our results into an overarching conclusion.

## 2. DATA: A NIHAO-UHD MILKY WAY ANALOGUE SIMULATION

For this project, we use a cosmological zoom-in simulation of a Milky Way analogue (g8.26e11) from the *Numerical Investigation of a Hundred Astronomical Objects* (NIHAO, Wang et al. 2015) suite. This model galaxy was calculated as part of the NIHAO-UHD project (Buck et al. 2020) and has previously been used in various works studying Milky Way satellites (Buck et al. 2019), Milky Way’s dark halo spin (Obreja et al. 2022), inferring birth properties of stars with abundance clustering (Ratcliffe et al. 2022), as well as the evolution of the interstellar medium’s radial metallicity gradient since redshift three (Ratcliffe et al. 2024).

Simulations were carried out with the smoothed particle hydrodynamics code Gasoline2 (Wadsley et al. 2017), including sub-grid turbulent mixing, using cosmological parameters from Planck Collaboration et al. (2014) with initial conditions and energetic feedback descriptions from the NIHAO project (Wang et al. 2015). Zoom-in simulations were then performed as described in detail by Buck et al. (2021) with star formation following Stinson et al. (2006) and energetic feedback following Stinson et al. (2013). We note that this is a slightly different rerun of the same simulation than the one studied by Buder et al. (2024b); in this work, we use a higher resolution version and updated chemical yields.

Because computational resources still limit the mass resolution of simulations, we are relying on tracer particles that represent simple stellar populations (SSPs) with the same age, overall metallicity and discrete initial mass function (IMF). Buck et al. (2021) have implemented the flexible chemical evolution code CHEMPY (Rybicki et al. 2017) to calculate the chemical yields for the SSPs. In particular, we use the alternative (alt) setup of CHEMPY that assumes a Chabrier (2003) IMF with high-mass slope of  $\alpha_{\text{IMF}} = -2.3$  over a mass range of  $0.1 - 100 M_\odot$  for SSPs across a metallicity range of  $Z/Z_\odot \in [10^{-5}, 2]$ . The code calculates the contribution from asymptotic giant branch (AGB) stars, CCSN across a mass range of  $8 - 40 M_\odot$ , and SNIa with an exponential function with exponent  $-1.12$ , a delay time of 40 Myr, and a normalization of the SNIa rate of  $\log_{10}(N_{\text{Ia}}) = -2.9$ . For each of these nucleosynthetic channels, yields from the following studies are used: Chieffi & Limongi (2004) for CCSN, Seitenzahl et al. (2013) for SNIa, and Karakas & Lugardo (2016) for AGB stars (new\_fit model in Buck et al. 2021). Contrary to a previous study by Buder et al. (2024b), we take the elemental abundances at face value and do not apply any shifts.

We limit the simulation data to the main halo by applying PYNBODY’s implementation of the Amiga Halo Finder (Knollmann & Knebe 2009) and then reposition and rotate this

main halo to be face-on based on the angular momentum with PYNBODY’s ANALYSIS.ANGMOM.FACEON module (Pontzen et al. 2013). We then further transform the resulting galactocentric Cartesian coordinate ( $X, Y, Z$ ) and velocities ( $V_X, V_Y, V_Z$ ) to Cylindrical ones as done in a previous study of this main halo by Buder et al. (2024b).

The model galaxy has a virial radius of  $R_{\text{vir}} = R_{200} = 206$  kpc and a total mass (gas, stars and dark matter) inside  $R_{\text{vir}}$  of  $9.1 \cdot 10^{11} M_\odot$ . At redshift zero, it contains  $8.2 \cdot 10^{11} M_\odot$  dark matter,  $6.4 \cdot 10^{10} M_\odot$  gas mass and  $2.3 \cdot 10^{10} M_\odot$  stellar mass with a stellar mass resolution of around  $7.5 \cdot 10^3 M_\odot$ . When using a fifth of the virial radius as a reference to calculate total luminosity<sup>1</sup> and mass, we estimate a half-light radius, that is, effective radius of  $R_e = 3.79$  kpc and a half-stellar-mass radius of 2.97 kpc.

To achieve a roughly similar selection as the observational data of the Milky Way (Genovali et al. 2014) and other galaxies (e.g. Chen et al. 2023), we restrict the simulation data to a galactocentric radius of  $R_{\text{Gal}} \leq 20$  kpc and  $|z| \leq 10$  kpc, as shown in Fig. 1. Similar to the Milky Way (Poggio et al. 2018; Lemasle et al. 2022), we note a warp of the stellar and gaseous disk (see Figs. 1b and 1e, respectively) leading to asymmetric deviations from the gas disk with a gas scale height of  $h_{z,\text{gas}} = 1.25$  kpc.

To avoid too strong effects of radial migration (Binney & Tremaine 2008; Frankel et al. 2018; Grand et al. 2016; Minchev et al. 2018) while maintaining a sufficiently large sample size we further enforce stars to be younger than 0.5 Gyr, corresponding to roughly the time of four galactic rotations, and being half the value found by Minchev et al. (2018) for very limited migration in the Milky Way. This selection defacto limits the vertical range of 99% of stars to  $|z| = 1.4$  kpc. The strong influence of this age cut on the vertical distribution of stars in the Milky Way analogue can best be appreciated from the difference of vertical density distributions of stars in Figs. 1b and 1c. We are applying these cuts for all following analyses of the radial metallicity gradient in Section 3.

## 3. THE LINEARITY OF THE RADIAL METALLICITY GRADIENT IN NIHAO-UHD

In this section, we analyse the functional shape of the radial metallicity gradient. To get a first impression of possible shapes, we show the face-on view of the decreasing radial metallicity gradient of the simulation in Figs. 2a (for young stars) and Fig. 2d (for gas). Foreshadowing the later parts of this work on local variations, we also show a linear radial fit to either distribution in Fig. 2b and 2e and show the fit residuals in Figs. 2c and 2f.

At the moment, however, we focus on the linearity and thus the logarithmic density distribution of star particle iron abundances [Fe/H] across different galactocentric radii  $R_{\text{Gal}}$ . This distribution is shown in Fig. 3a and strongly suggests that the gradient is predominantly linear, similar to findings for the Milky Way. More complex shapes, such as piecewise linear ones have been suggested based on incomplete and limited data in the literature. We are thus also analysing these shapes with the complete and better-sampled data points of the NIHAO-UHD simulation. We firstly test different global fits in Section 3.1, before testing the influence of binning and coverage in Sections 3.2 and 3.3, respectively.

<sup>1</sup> Using PB.ANALYSIS.LUMINOSITY.HALO\_LUM (Pontzen et al. 2013).

TABLE 1  
GLOBAL LINEAR GRADIENT FIT RESULTS WITH DIFFERENT METHODS.  
LINEARREGRESSION IS PART OF THE SKLEARN PACKAGE.

Method	Intercept ( $a_0 \pm \sigma_{a_0}$ )	Slope ( $a_1 \pm \sigma_{a_1}$ )
STATSMODELS.API.ODR	$0.46266 \pm 0.00039$	$-0.04109 \pm 0.00005$
SCIPY.ODR	$0.46268 \pm 0.00039$	$-0.04109 \pm 0.00005$
NP.POLYFIT	$0.46266 \pm 0.00039$	$-0.04109 \pm 0.00005$
LINEARREGRESSION	$0.46286 \pm 0.00028$	$-0.04114 \pm 0.00008$
SCIPY.CURVE_FIT	$0.46266 \pm 0.00039$	$-0.04109 \pm 0.00005$

### 3.1. Global gradient fits

We fit three different functional forms to the global data: a linear function (used for Fig. 2b)

$$f_{\text{lin}}(R_{\text{Gal.}}) = c_1 \cdot R_{\text{Gal.}} + c_2, \quad (1)$$

a piecewise linear with a break radius  $R_{\text{break}}$

$$f_{\text{piece}}(R_{\text{Gal.}}) = \begin{cases} c_1 \cdot R_{\text{Gal.}} + c_2 & \text{if } R_{\text{Gal.}} \leq R_{\text{break}} \\ c_3 \cdot R_{\text{Gal.}} + c_4 & \text{if } R_{\text{Gal.}} > R_{\text{break}}, \end{cases} \quad (2)$$

and a quadratic function

$$f_{\text{quad}}(R_{\text{Gal.}}) = c_1 \cdot R_{\text{Gal.}}^2 + c_2 \cdot R_{\text{Gal.}} + c_3. \quad (3)$$

The coefficients of the functions are fitted with the SCIPY.OPTIMIZE function CURVE\_FIT (Virtanen et al. 2020) and listed in Table 2. To estimate the uncertainty of the break radius  $R_{\text{break}}$ , we use the profile likelihood method to identify the radii at which the residual sum of squares (RSS) values are increased by  $1\sigma$  from the best RSS radius in steps of  $\Delta R_{\text{break}} = 0.1$  kpc and 0.5 kpc for the full and binned data set, respectively. We compute the RSS for each model  $f_i$  (see Eqs. 1-3) based on the  $N$  data points as

$$\text{RSS}_i = \sum_{n=1}^N ([\text{Fe}/\text{H}]_n - f_i(R_{\text{Gal.},n}))^2. \quad (4)$$

We have confirmed the robustness of our fits by applying other fitting routines as outlined in Table 1. After fitting three different functional forms, we use a combination of parameters to determine which model provides the best fit.

In Table 2, the RSS value is the smallest (although only by a small margin) for the quadratic function. When assuming  $\sigma^2 = \text{RSS}/N$ , we can also define a logarithmic likelihood

$$\ln L = -\frac{N}{2} \ln(2\pi) - \frac{N}{2} \ln \frac{\text{RSS}}{N} - \frac{N}{2} \quad (5)$$

for the  $N$  data points. For  $k$  free parameters, we then calculate the Akaike Information Criterion (AIC) and the Bayesian Information Criterion (BIC) as

$$AIC = 2k - 2 \ln L \quad BIC = k \ln N - 2 \ln L. \quad (6)$$

For these criteria, the quadratic function performs slightly better than the linear or piecewise linear functions (see Table 2).

We show the fit residuals in Fig. 3b as density distribution as well as in Fig. 3c as percentile distributions in radial bins of  $\Delta R_{\text{Gal.}} = 0.5$  kpc. While the density distribution shows substructure, which we investigate later in Section 4, we note an increase in the median residuals of the linear fit in Fig. 3c towards the inner and outer radii, especially for  $R_{\text{Gal.}} > 17$  kpc. A quadratic fit (see orange lines in Fig. 3) results in a slightly steeper linear component of the gradient (from  $-0.0411$  to  $-0.0497$  dex kpc $^{-1}$ ), which is counteracted by the quadratic flattening term of  $+0.0005$  dex kpc $^{-2}$ . The latter leads to an

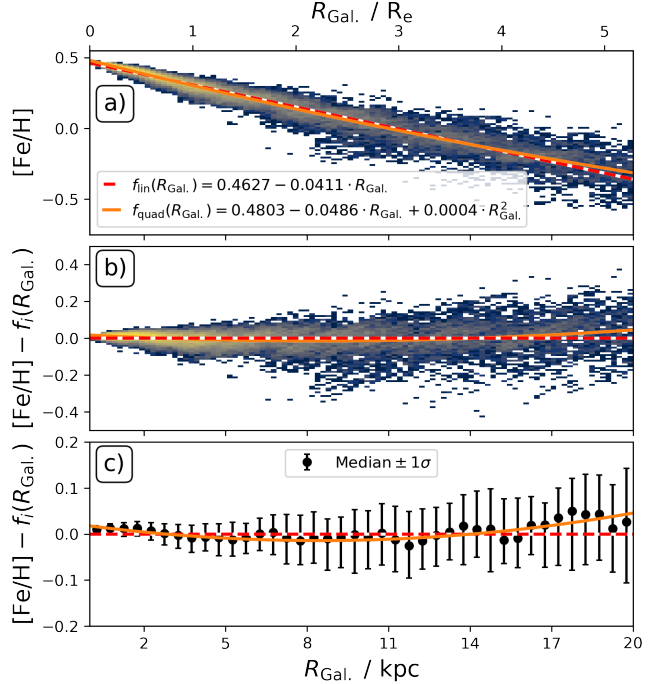


FIG. 3.— Global fits and deviation to the radial metallicity gradient  $R - [\text{Fe}/\text{H}]$ . Functional forms of the linear (red) and quadratic (orange) lines are shown in the legend. Panel a) shows the underlying data of all data points as logarithmic density and the global fit to them as red dashed line. Panel b) shows the deviation of data from a linear gradient as a logarithmic density plot, whereas panel c) shows the 16th and 84th percentile around the median deviation as error bars in  $\Delta R_{\text{Gal.}} = 0.5$  kpc bins.

effective flattening of  $-0.172 + 0.200 = 0.028$  dex (linear vs. quadratic terms) at  $R_{\text{Gal.}} = 20$  kpc. While seemingly only a nuisance correction across the large extent of  $[\text{Fe}/\text{H}]$  and  $R_{\text{Gal.}}$ , this quadratic function outperforms the linear fit. This is most apparent in Fig. 3c, where the orange line better traces the median residuals from the linear function across all radii. This suggests that non-linear functions, such as piecewise linear or quadratic ones describe the gradient better.

Distinguishing between the two latter functional forms is challenging. The quantitative performance indicators—RSS, AIC, and BIC—show very similar values for both forms, and a closer examination of the residuals in Fig. 4 reveals no clear visual advantage for either the piecewise linear or quadratic model.

**When only fitting data up to  $R_{\text{gal}} < 10$  kpc, we note that the linear fit performs as well as the other forms, suggesting that the inner disk ( $R_{\text{gal}} < 10$  kpc) is indeed showing a linear trend, with non-linear behavior only being imprinted in the outer disk.**

**TAKE-AWAY:** Both piecewise linear and quadratic functions provide a better fit to the radial metallicity relation than a simple linear model. However, based on our assessments, there is no clear preference between the piecewise and quadratic functions **and a linear function behaves as well as the other forms for the innermost 10 kpc**.

### 3.2. The influence of binning

In this section, we test the influence of fitting a function to all points of the distribution or binned data in steps of  $\Delta R_{\text{Gal.}} = 0.5$  kpc, using median values as data points and

TABLE 2

FIT EVALUATION OF LINEAR, QUADRATIC, AND PIECEWISE LINEAR FITS. EXTRA PARAMETERS ARE QUADRATIC TERM AND BREAK RADIUS FOR THE QUADRATIC AND PIECEWISE FIT. RSS STANDS FOR RESIDUAL SUM OF SQUARES (EQ. 4). AIC STANDS FOR AKAIKE INFORMATION CRITERION AND BIC STANDS FOR BAYESIAN INFORMATION CRITERION (SEE EQ. 6).

Function	Intercept ( $a_0 \pm \sigma_{a_0}$ )	Slope ( $a_1 \pm \sigma_{a_1}$ )	Extra Parameter	RSS	AIC	BIC
Linear	$0.46266 \pm 0.00039$	$-0.04109 \pm 0.00005$	—	87.0	-118270	-118260
Quadratic	$0.48031 \pm 0.00055$	$-0.04864 \pm 0.00018$	$0.00045 \pm 0.00001$	82.7	-120150	-120120
Piecewise	$-0.04477 \pm 0.00010$	$0.47473 \pm 0.00047$	—	82.9	-120090	-120050
	—	$-0.03562 \pm 0.00014$	$9.3 \pm 0.1$			
Linear (bins)	$0.46983 \pm 0.00567$	$-0.04146 \pm 0.00127$	—	0.0167	-190	-190
Quadratic (bins)	$0.47457 \pm 0.00674$	$-0.04585 \pm 0.00359$	$0.00031 \pm 0.00024$	0.0056	-240	-230
Piecewise (bins)	$-0.04336 \pm 0.00188$	$0.47274 \pm 0.00606$	—	0.0052	-240	-230
	—	$-0.03360 \pm 0.00589$	$11.50 \pm 0.25$			

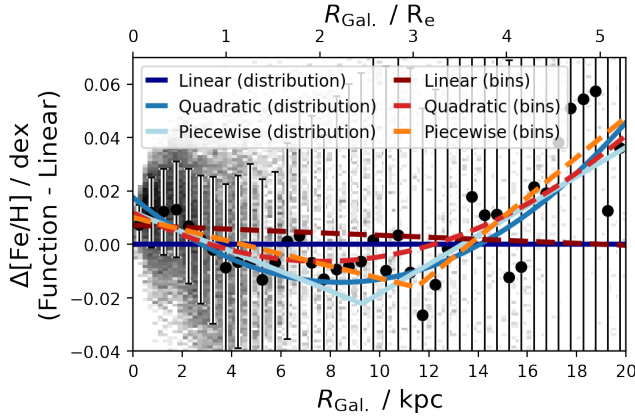


FIG. 4.— Deviation of different radial metallicity gradient functions from the global linear fit. Shown are the different functions (linear, quadratic, and piecewise linear) estimated from the full distribution (solid lines) or medians and standard deviations (error bars) in  $\Delta R_{\text{Gal.}} = 0.5$  kpc bins (dashed lines).

standard deviations<sup>2</sup> as uncertainty (see also Hemler et al. 2021, who fitted functions to radially binned IllustrisTNG data). The results are shown in Fig. 4. Given that more than half of the young star particles of the galaxy are within  $R_{\text{Gal.}} < 4$  kpc as well as a height below  $h_{z,\text{gas}} = 1.25$  kpc, this binning – although counteracted by the smaller spread of [Fe/H] in the inner galaxy – weighs the distribution of the inner galaxy significantly less than when weighing all particles equally (20 vs. 34 000 data points). The parameters fitted to the binned data exhibit a larger uncertainty due to our use of the spread of [Fe/H] per bin as absolute uncertainty  $\sigma$ , but the fitted parameters agree well within the fitting uncertainties.

**TAKE-AWAY:** While the specific slopes differ when fitting all points or binned data, they agree within the small fitting uncertainties.

### 3.3. The influence of radial coverage on linear fits

Although we have gained useful insight into the global function, observational data will rarely cover the full extent of the stellar disk. Milky Way studies have previously been limited to the range of around 5 – 15 kpc. There are often similar limitations and even gaps in extragalactic data. Using smaller ranges, observational studies have found hints of piece-wise linear gradients with a break radius in them based on limited radial coverage (e.g. Andrievsky et al. 2002a; Yong et al. 2012; Boeche et al. 2013; Hayden et al. 2014; Anders et al. 2017; Donor et al. 2020; Chen et al. 2023). These results

<sup>2</sup> We note that this  $\sigma$  is not equivalent to observational uncertainty and can thus not be directly applied onto observational analyses.

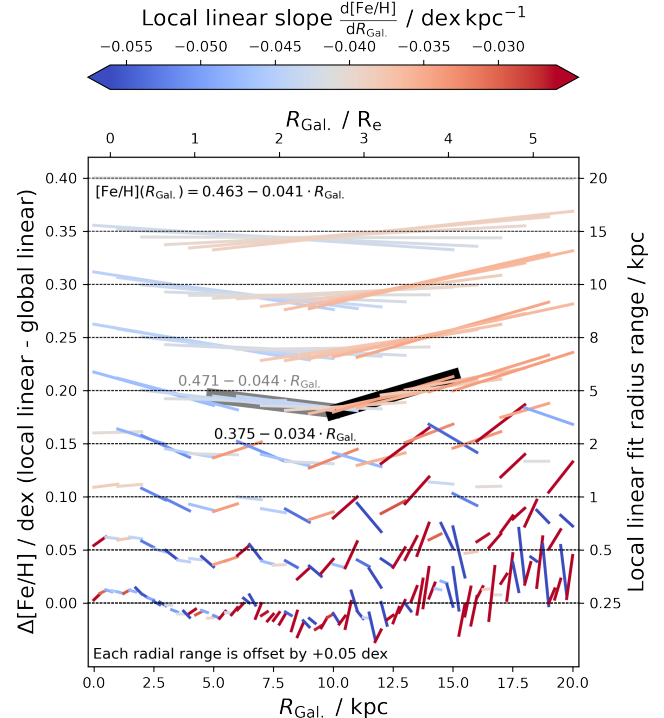


FIG. 5.— Impact of different coverage in galactocentric radius when fitting a linear radial metallicity gradient to young stars. Each horizontal segment uses a different running radial fitting range between 0.25 and 15 kpc as outlined on the right. For better contrast, the global linear fit is subtracted from the local gradient estimates and each line is colored by the gradient slope with a color scale centered around the global fit slope. Additionally, the slope of each line segment highlights the difference between global and local slopes. Thus, if the local fit exactly matches the global fit, we display it as a flat line (zero slope difference) on top of the gray dashed line (zero offset deviation) and give it a gray color signaling the same gradient value as the global fit.

are intriguing, since a quadratic function can, to first order, be approximated by two linear functions with a break radius. We therefore want to use our simulation to test if the radial coverage may indeed delude us into identifying broken linear gradients.

We test how smaller coverage and piecewise linear fits could mimic a complex global gradient by fitting in piecewise linear radial ranges of 0.25, 0.5, 1, 2, 5, 8, 10, 15, and 20 kpc. We show their difference with respect to a global linear fit in Fig. 5, with color-coding indicating the slope of the local gradient. A horizontal dashed line indicates the same slope as the global fit, whereas the offset of a line from the said horizontal dashed line indicates the local deviation from the global gradient intercept. Differences in line slopes are visualising the difference in gradient slopes between the global and local

fits. We see that all ranges suggest more or less significant deviations from a global linear fit. The innermost fit suggests a significantly different gradient than the outermost fit. We also note increasing slope differences towards the smallest scales, hinting at local deviations from a global pattern. We follow these up in Section 4, but for now, focus on the larger-scale trends.

When directly comparing an inner and outer radius fit, such as between  $R_{\text{Gal.}} = 5 - 10 \text{ kpc}$  (thick grey line in Fig. 5) and  $R_{\text{Gal.}} = 10 - 15 \text{ kpc}$  (thick black line in Fig. 5), we note a significant change, similar to previous estimates of the Milky Way (e.g. Yong et al. 2012; Lemasle et al. 2008). In our case, the gradient estimate changes from  $[\text{Fe}/\text{H}](R_{\text{Gal.}}) = 0.471 - 0.044 \cdot R_{\text{Gal.}}$  to  $[\text{Fe}/\text{H}](R_{\text{Gal.}}) = 0.375 - 0.034 \cdot R_{\text{Gal.}}$ . When looking at linear gradient fits across the radial coverage of  $\Delta R_{\text{Gal.}} = 5 - 15 \text{ kpc}$  in Fig. 5, the gradient is steeper (bluer color) for smaller radii and flatter (redder) for larger radii. Indeed, a piecewise linear function can well mimic a complex global gradient.

We note that in the simulated data, we see local deviations that become traceable below  $\Delta R_{\text{Gal.}} \leq 2 \text{ kpc} \sim 0.5 R_e$  (bottom part of Fig. 5). This might indicate the spatial resolution required to see local effects, such as spiral arms, for extragalactic studies (see also Krumholz & Ting 2018; Li et al. 2024). We pursue this observation in the following Section 4.

**TAKE-AWAY:** We find that a piecewise linear function can well mimic a quadratic function across the scales used in Milky Way and extragalactic studies. Local deviations become traceable below a spatial resolution of  $\Delta R_{\text{Gal.}} \leq 2 \text{ kpc}$  (or  $\Delta R_{\text{Gal.}} \leq 0.5 R_e$ ).

#### 4. SCATTER AND LOCAL DEVIATIONS FROM THE GRADIENT

Now that we are sufficiently satisfied that our flattening gradient function reproduces the overall shape of the radial metallicity gradient, we are concerned with both the scatter and local slope deviations across the galactocentric radii in this section. In detail, we analyse the scatter (Section 4.2), vertical variations (Section 4.2), azimuthal variations (Section 4.3, particularly motivated by the localised, spiral-shaped fit residuals of Figs. 2c and 2f) and deviations across different ages (Section 4.4).

##### 4.1. Scatter

When investigating the change in scatter from the innermost radii to the outermost (see Fig. 3c), we see a steady increase in  $1 - \sigma$  spread. This spread increases from  $\sigma[\text{Fe}/\text{H}] = 0.01 \text{ dex}$  at  $R_{\text{Gal.}} = 0.25 \pm 0.25 \text{ kpc}$  to  $\sigma[\text{Fe}/\text{H}] = 0.06 \text{ dex}$  at  $R_{\text{Gal.}} = 8.25 \pm 0.25 \text{ kpc}$  and reaches  $\sigma[\text{Fe}/\text{H}] = 0.10 \text{ dex}$  at  $R_{\text{Gal.}} = 19.75 \pm 0.25 \text{ kpc}$ .

When we recall the observed significant spread in metallicities of young open clusters at the solar radius beyond observational uncertainty (e.g. Donor et al. 2020; Spina et al. 2021) and our selection of only young ( $< 0.5 \text{ Gyr}$ ) stars from the simulation, a strong impact of this scatter by radial migration should be excluded. At this point, we can imagine that this chemical diversity might be caused by less well-mixed gas or non-radial effects (such as vertical or azimuthal ones), which we investigate subsequently.

##### 4.2. Vertical deviations

In this section, we now look at deviations with respect to the vertical dimension, that is,  $R - z$ . In Fig. 6 we show the

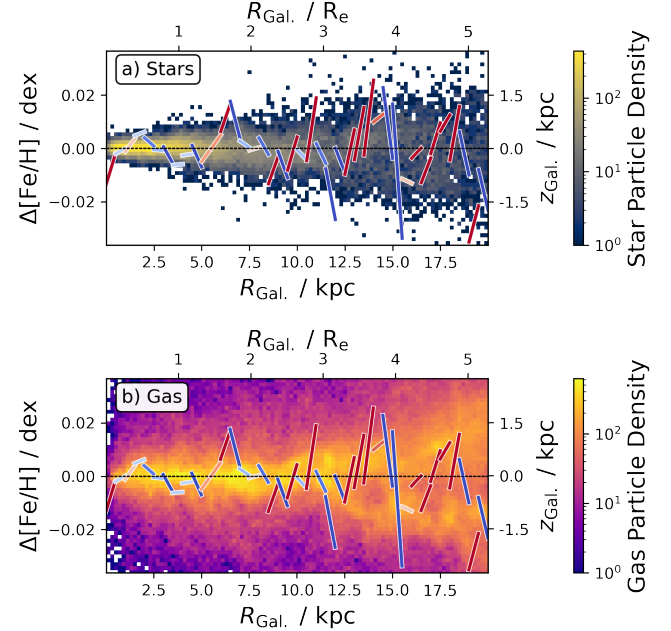


FIG. 6.— Local gradient deviations (red-blue lines) similar to the second lowest row of Fig. 5 for radial gradients in 0.5 kpc steps (but compared to a global quadratic function) overlapped on top of the logarithmic density distribution in  $R - z$  for  $|z| < 3 \text{ kpc}$  of gas (panel a) and stars (panel b). We see no strong correlation between local gradient slopes (red-blue lines) and star or gas density in this projection.

previously identified local gradient deviations (lines following the left axis label) on top of the vertical density distribution ( $R - z$ ) of young stars (Fig. 6a) and gas (Fig. 6b) between  $-3 < z < 3 \text{ kpc}$ . Although the quickly decreasing number of young stars (Fig. 6a) at outer radii does not show substructure in the density plots for reasonable bin sizes, we see more substructure for the gaseous component in Fig. 6b). In particular, we see rather minor deviations at small radii (where most stars and gas are close to the plane). At increasing radii, we notice an increase in both the vertical distribution of stars, and increasing local gradient deviations. In particular, we note a significant deviation of the slope around  $R_{\text{Gal.}} \sim 15 \text{ kpc}$ , where the gradient deviation line is steep and blue (indicating a much steeper gradient at this radius), and we notice a significant overdensity of gas around  $z \sim 1 \text{ kpc}$ . Overall, however, we do not see strong correlations in this particular plane.

This could, however, be caused by a super-position effect of the up- and downturn at larger radii due to the galactic warp (see Figs. 1b and 1e). Although the warp of the stellar disk in Fig. 1b is not as clear, we confirm that both the gas disk and the youngest stars below 0.5 Gyr are tracing each other across the simulation in both galactocentric radius  $R_{\text{Gal.}}$  and height  $z_{\text{Gal.}}$  for different sectors in the azimuthal direction. We note that the superposition in Fig. 6 could smear out local correlations of slope changes with gas overdensities, for example, by spiral arms. Although such an edge-on view of the galaxy may indeed be the only observable one for extragalactic targets, for example, of the GECKOS survey of edge-on galaxies (van de Sande et al. 2023), we have the luxury of being able to analyse the azimuthal direction of our simulated galaxy, too.

**TAKE-AWAY:** We see no strong correlations of deviations in the vertical direction throughout the simulation. Such correlations could, however, be blurred by azimuthal effects, like the galactic warp, which needs to be disentangled in the azimuthal

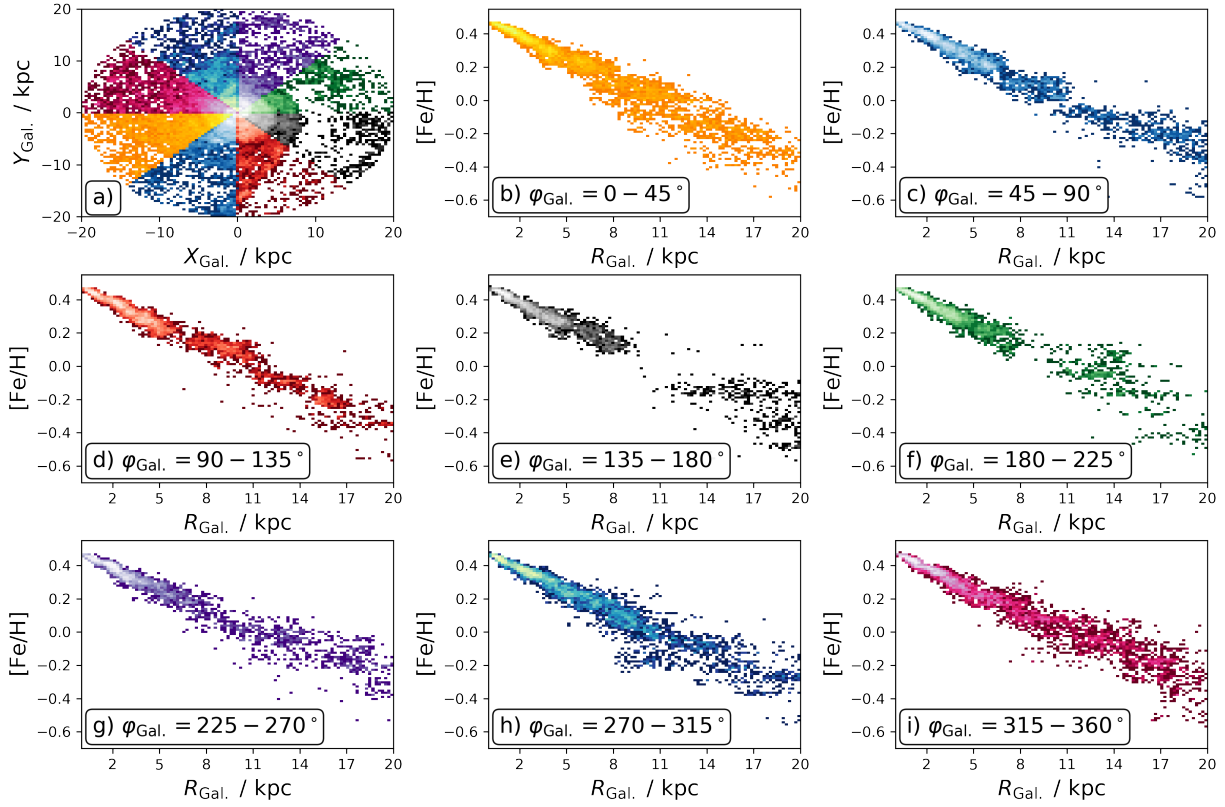


FIG. 7.— Stellar density variation across 8 different sectors (with color-code visualised in panel a) of the radial metallicity gradient  $R - [\text{Fe}/\text{H}]$  across 8 different azimuth ranges (panels b-i). A rotating lighthouse-like GIF animation of the median age and median density of the  $R - [\text{Fe}/\text{H}]$ -relation across different azimuths is freely available on a [repository](#).

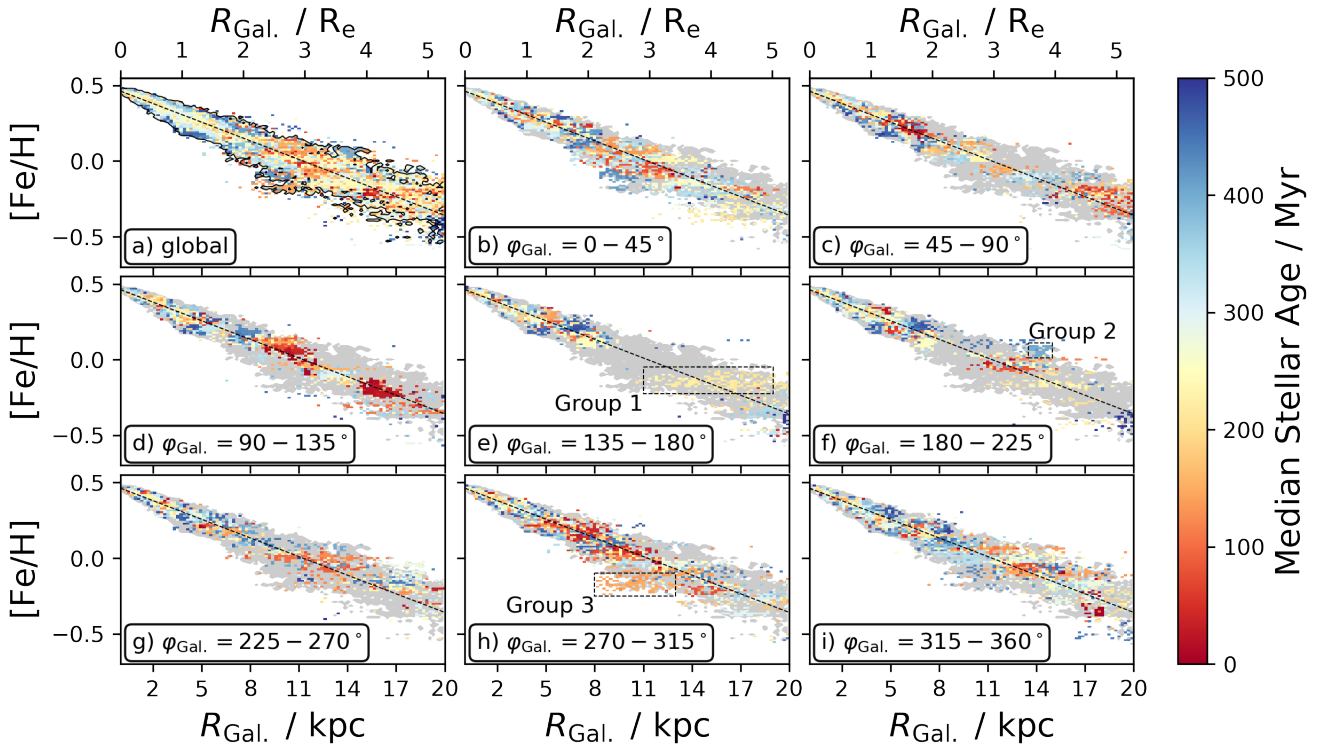


FIG. 8.— Same as Fig. 7, but colored by median age per bin. We identify 3 groups with boxes in panels e, f, and h. A rotating lighthouse-like GIF animation of the median age and median density of the  $R - [\text{Fe}/\text{H}]$ -relation across different azimuths is freely available on a [repository](#).

dimension.

#### 4.3. Azimuthal deviations

To analyse the deviations from a global gradient across different azimuthal viewing angles, we divide the galaxy into 8 sectors with  $\Delta\varpi_{\text{Gal.}} = 45^\circ$  (see Fig. 7a). This allows us to study the positions around the upturn and downturn of the galactic warp with the median azimuth of young star particles below and above the plane being  $\varphi_{\text{Gal.}} \sim 183^\circ$  and  $\varphi_{\text{Gal.}} \sim 4^\circ$ , respectively (see Fig. 1e), while maintaining a reasonable sample size.

At face value, the distribution of  $R_{\text{Gal.}} - [\text{Fe}/\text{H}]$  for each sector follows a similar, rather linear shape with most stars being born in the inner 5 kpc of the galaxy. However, we find significant deviations in different sectors of the galaxy (Fig. 7). On the one hand, we find non-linear deviations as bumps with slightly increased or decreased iron abundance – up to  $0.1 - 0.2$  dex – in Figs. 7c at  $R_{\text{Gal.}} \sim 18$  kpc, 7d at  $R_{\text{Gal.}} \sim 10$  kpc, 7f at  $R_{\text{Gal.}} \sim 14$  kpc, and 7g at  $R_{\text{Gal.}} \sim 17$  kpc. On the other hand, we find significant gaps in the distribution at similar  $[\text{Fe}/\text{H}]$ , most strikingly at the upturn of the galactic warp in Fig. 7e ( $\varpi_{\text{Gal.}} = 135 - 180^\circ$ ) at  $[\text{Fe}/\text{H}] \sim 0$  dex and  $R_{\text{Gal.}} \sim 8 - 14$  kpc. We note that the sector e) with the gap is surrounded by two sectors (d and f) with significant overabundance at the same radius. This could be indicative of stars having formed as a result of gas moving from sector e towards either azimuthal direction, causing a gas overdensity which could in turn lead to higher star formation activity. To establish this observation, we take a closer look at the time-domain, that is, stellar age as well as the spatial domain of  $R_{\text{Gal.}} - \varphi_{\text{Gal.}}$  in the next section.

**TAKE-AWAY:** We find various deviations from the global trend in the azimuthal direction, including gaps and isolated streaks of stars with similar  $[\text{Fe}/\text{H}]$  throughout  $\Delta R_{\text{Gal.}} = 2 - 6$  kpc. These can introduce local over- and under-enhancement of up to  $\pm 0.2$  dex in  $[\text{Fe}/\text{H}]$  at a given radius. In the next section, we analyse whether the stars of these streaks have been born at the same or different time.

#### 4.4. Deviations with time and age

In this section, we examine the radial metallicity gradient in a small age range less than 0.5 Gyr. To do so, we color Fig. 7 by the median stellar age rather than the logarithmic density in Fig. 8. We find an overall significant scatter across time, suggesting a good mix of star formation across all sectors for stars born within less than 0.5 Gyr. For stars within this restricted age range, we do not see a strong correlation with radius, such as older stars being born further inside, but a larger amount of stars being born closer to the galactic centre. We note that stars with similar  $[\text{Fe}/\text{H}]$  in each sector tend to be formed at similar times (within 50 Myr), that is, as flat lines with the same color (age) in Figs. 8b-i. To guide the eye, we have identified Group 1 in Fig. 8e (around  $R_{\text{Gal.}} \sim 14$  kpc at  $\varpi_{\text{Gal.}} = 180 - 225^\circ$ ). We further note that the enriched bumps identified earlier are born at similar times, see, for example, Group 2 in Fig. 8f. The coloring by age also reveals that stars with lower  $[\text{Fe}/\text{H}]$  than expected (see Group 3 in Fig. 8h) are born at similar times. In some cases, these extend to  $\Delta R_{\text{Gal.}} = 2 - 6$  kpc, see Groups 1, 2, and 3 in Fig. 8. At a given radius  $R_{\text{Gal.}}$ , these streaks cause a significant spread in local  $[\text{Fe}/\text{H}]$  of up to  $\pm 0.2$  dex (see Fig. 8).

From the analysis of azimuthal sectors, the impression arose that the star formation in this simulated Milky Way analogue is

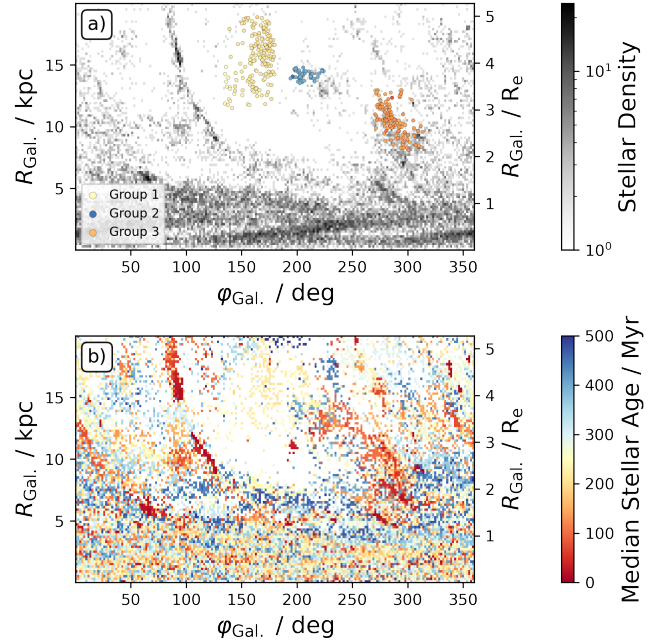


FIG. 9.— Density distribution (panel a) and age distribution (panel b) of young stars in the azimuthal and radial direction  $\varphi_{\text{Gal.}} - R_{\text{Gal.}}$ . In panel a), we also show the groups previously identified in Fig. 8.

– as expected for a spiral galaxy – rather patchy and localised on the smallest timescales. This is confirmed by looking at the spatial distribution of azimuth  $\varphi_{\text{Gal.}}$  and radius  $R_{\text{Gal.}}$  in Fig. 9. Already when looking at the density distribution of all stars born within less than 0.5 Gyr in Fig. 9a, multiple streams are visible, stars on spiral patterns (see also Kreckel et al. 2019; Chen et al. 2024b). **We note for example a narrow sequence around  $\varphi_{\text{Gal.}} \sim 100$  deg stretching along  $R_{\text{Gal.}} = 8 - 20$  kpc visible as significant overdensity in Fig. 9a and distinctly red (young) sequence in Fig. 9b. This sequence coincides with the red features in Fig. 8d, which follow the linear metallicity gradient very closely.** When following up the previously identified Groups 1, 2, and 3, we recover them on said spiral patterns (Groups 1 and 3) or a local overdensity (Group 2). Although one could imagine that radial migration might induce such a spiral-like shape for the stars of groups 1 and 3, their low age of less than 250 Myr would require a significant migration effect of several kpc, while having no influence on the older stars of group 2. When tracing the position of significant overdensities from Fig. 9a in the same projection colored by age in Fig. 9b, we note that for radii above  $R_{\text{Gal.}} > 5$  kpc these overdensities are colored in red, that is, containing indeed young stars with ages below 200 Myr and being consistent with the most recent star formation along these spiral patterns in the outer galaxy.

**TAKE-AWAY:** We find significant scatter across the radial metallicity distribution caused by streaks of stars born with similar  $[\text{Fe}/\text{H}]$  at similar times (within 50 Myr) across either very local or radially extended spiral-shaped regions of the galaxy, suggesting local enhancement patterns in small overdensities or along spiral arms.

## 5. DISCUSSION

Having presented the analysis, we now put our results into the context of other work in terms of our initial aims: to analyse the shape (Section 5.1), scatter (Section 5.2), local

deviations (Section 5.3), and time-dependence (Section 5.4) of the radial metallicity gradient. These initial discussions inform our thoughts on the implications of this work for Milky Way studies in Section 5.5 and the studies of other galaxies in Section 5.6.

### 5.1. Linearity of the radial metallicity gradient

The radial metallicity gradient of our simulated NIHAO-UHD Milky Way analogue showed an overall decreasing, predominantly linear shape, as established in Section 3. Motivated by previous works by Sánchez-Menguiano et al. (2016), among others, we also fitted piecewise linear and quadratic functions to the data in Section 3.1. Both forms perform better than a linear trend. The very similar fitting performances indicate no significant preference between either piecewise linear or quadratic function. Due to both functions' rather good overall fit, we have not tried more exotic non-linear functions as done by Scarano & Lépine (2013). Increasing the flexibility of the gradient function could, however, improve the fit at the innermost kpc, where a flattening is predicted by our simulation, but chemical enrichment is also harder to simulate (see also Minchev et al. 2013; Sun et al. 2024). We have found no significant influence of binning for our gradient estimates (Section 3.2), but have found that a limited radial coverage - as is the case for the Milky Way - could mimic a truly quadratic function with two piecewise linear fits (Section 3.3). This is important, as it has significant implications for the conclusions we draw from the incomplete data of our Milky Way, as we will discuss in more detail in Section 5.5.

The balance between a quadratic and piecewise linear radial metallicity gradient teeters at the breaking radius. If present, our analysis of the Milky Way analogue would place it **at**  $R_{\text{break}} \sim 9.3 - 11.5 \text{ kpc}$ . This radius is strikingly close to the radius of 9 kpc found by Hemler et al. (2021) for a TNG50 galaxy simulation with a stellar mass of  $\log(M_{\star}/M_{\odot}) = 10.72$ , that is, close to the Milky Way's (see their Fig. 2). In terms of physical reasons for a breaking radius at this location, a direct and secular influence of a stellar bar with non-symmetric effects around the corotation radius (Di Matteo et al. 2013; Scarano & Lépine 2013) should be minor for our specific scenario due to the low ages of the stars considered in our analysis. In particular, our identified break radius is significantly larger than the corotation radius of the Milky Way bar at 4.5 – 7.0 kpc (Bland-Hawthorn & Gerhard 2016, and references therein) anyway. We are intrigued, however, by the proposition by Garcia et al. (2023) of galactic discs consisting of a star-forming inner disc with a steep gradient and a mixing-dominated outer disc with a flat gradient, with the break radius marking the region of transition between them. In Illustris TNG50-1 data, they found such a transition and break radius to be situated much further out at 30 kpc for Milky Way mass galaxies ( $10.1 \leq \log(M_{\star}/M_{\odot}) \leq 10.6$ ). While our best-fitting break radius - if present - is inconsistent with theirs, we will follow this up in more detail in Section 5.6, where we also discuss the implications for extragalactic studies in general.

### 5.2. Scatter of the radial metallicity gradient

In Section 4.1 we found an increasing scatter from  $\sigma[\text{Fe/H}] = 0.01 \text{ dex}$  in the inner galaxy to  $\sigma[\text{Fe/H}] = 0.10 \text{ dex}$  around  $R_{\text{Gal.}} \sim 20 \text{ kpc}$ . Comparing these values with simulations other than TNG50 with a similar metallicity spread (see Fig. 2 by Hemler et al. 2021) is rather difficult, as the literature focuses on the shape and density distribution (see

e.g. Minchev et al. 2014, their Fig. 10). When comparing with Milky Way studies (e.g. Anders et al. 2017), the scatter in the simulation is smaller than the observed spread of [Fe/H]. This can be visually appreciated by comparing the combinations of different measurements in the Milky Way (Genovali et al. 2014; Spina et al. 2021; Myers et al. 2022) in Fig. 10a and our simulation in Fig. 10b and c. We discuss the implications of this on studies of the Milky Way's gradient in Section 5.5.

When assuming that young star and gas phase abundances are similar, we find comparable scatter of abundances for example with respect to TYPHOON observations by Chen et al. (2023). To test this assumption, we also show the gas phase metallicity in Fig. 11, for which we find a similar shape and scatter of the gradient, but systematically less scatter or spread than observed gas phase abundance, thus urging us to treat the absolute values of abundances and abundance scatters as well as spreads with caution. We furthermore note that the spread of abundance in observations does only increase for some but not all of the observed (and thus observationally limited) galaxies by Chen et al. (2023). This potentially limits the range of galaxies to which our conclusions may apply. While the simulated abundance scatter is consistent with the predictions by the theoretical forced-diffusion model by Krumholz & Ting (2018), that is, a scatter of  $\sim 0.1 \text{ dex}$  over timescales of  $\sim 100 - 300 \text{ Myr}$ , our simulations suggest that the scatter is driven by the radial structure and large-scale spiral arms, which were not included in their model.

### 5.3. Localised vertical and azimuthal deviations and their correlation with gas

In Sections 4.2 and 4.3 we established that local deviations contribute significantly to the spread of the global metallicity gradient above  $R_{\text{Gal.}} > 8 \text{ kpc} \sim 2 R_{\text{e}}$ . We noted in particular a void of stars where we found an upturning warp of the galaxy around  $\varphi_{\text{Gal.}} \sim 180^\circ$  spatially close to regions of the galaxy (Groups 1 and 2) that deviated most significantly from the overall trend in Fig. 8 and Fig. 9.

These stellar voids pose the question if they are also void of gas thus suggesting the gas has shifted to the more enhanced regions. In Fig. 12 we are thus tracing both the spatial distribution of gas as colored density distribution and stars as grey contour lines and gas. We find that while stars and gas trace each other in the vertical direction, we do not always see a match between the two tracers in the radial direction. In particular, we do find a significant amount of gas around the stellar void of  $\varphi_{\text{Gal.}} \sim 180^\circ$  and  $R_{\text{Gal.}} \sim 8 - 11 \text{ kpc}$  in Figs. 12e and 12f. This gas seems to be more tightly concentrated though for example in the tight wave around  $R_{\text{Gal.}} \sim 8 - 11 \text{ kpc}$  in Fig. 12e. We also note that significant gas overdensities, for example around  $\varphi_{\text{Gal.}} \sim 0 - 45^\circ$  and  $R_{\text{Gal.}} \sim 7 \text{ kpc}$  in Fig. 12a do not seem to correlate with significant overenhancement in iron abundance (compare to Fig. 7a). While we see a hint of a coinciding deviation of  $\Delta[\text{Fe/H}]$  for larger deviations from the galactic plane  $\Delta z$  in the upturning outer region of Fig. 12f, this does not seem to be the case for the downturned outer region of Figs. 12b and 12i.

As the edge-on projection is not providing conclusive insights, we are now looking into the phase-on projection in Fig. 13. We have chosen a region of the simulated galaxy whose gas density at solar radius (Fig. 13c) matches with the recently measured distribution of young stars in the Milky Way at face value (Fig. 13a) by Poggio et al. (2021). Comparing simulated gas and observed young stars is preferable in this case, as the density of simulated stars is too low to easily

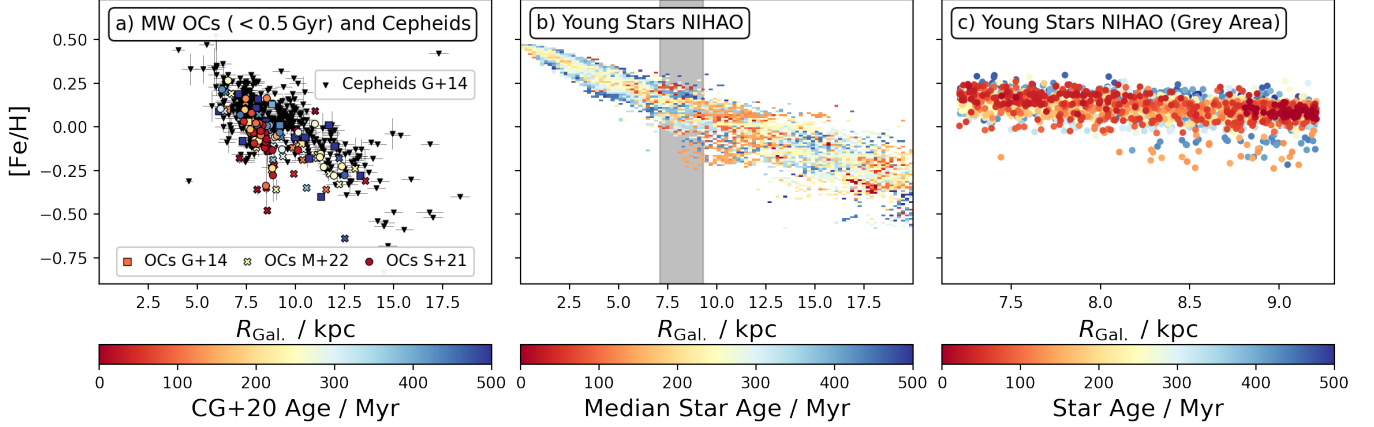


FIG. 10.— Comparison of the Milky Way’s radial metallicity trend as traced by Cepheids (black triangles, compiled from literature by Genovali et al. 2014, G+14) as well as young ( $<0.5$  Gyr) open cluster of the Milky Way as traced by the literature compilation from Genovali et al. (2014, G+14 as squares), APOGEE DR17 from Myers et al. (2022, M+22 as crosses), and GALAH DR3 from Spina et al. (2021, S+21 as circles). The latter two are compiled based on the membership and age catalogue by Cantat-Gaudin & Anders (2020, CG+20).

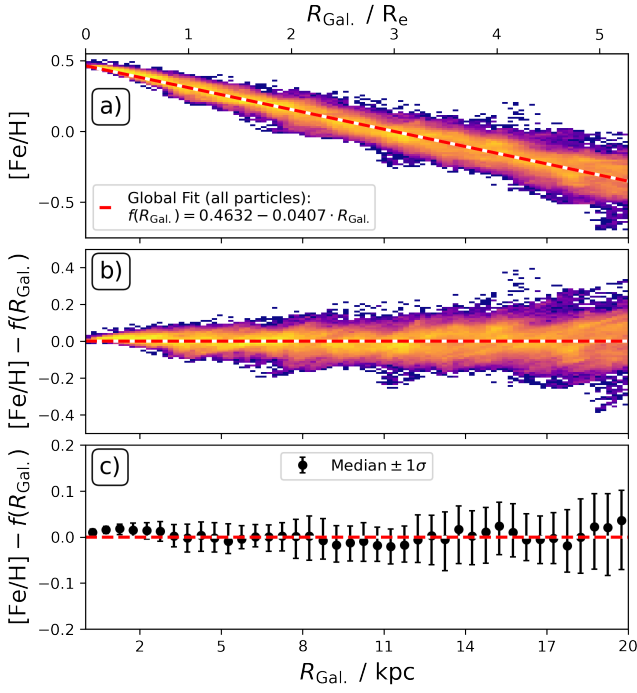


FIG. 11.— Same as Fig. 3, but for gas.

identify overdensities (Fig. 13b). The region and its gas spiral structures appear to be representative, as these structures exist throughout the whole galaxy (see Fig. 1d).

In the different panels of Fig. 14, we thus show this representative region of the galaxy, but color each spatial bin by stellar metallicity (Fig. 14a), the deviation from the global linear trend (Fig. 14b) as well as the gas metallicity (Fig. 14c) and its deviation from the global linear trend (Fig. 14d). In all cases, we also overlay the density contours of the significant gas overdensities (red regions in Fig. 13c). As expected, we see that the metallicity color map of the stars in Fig. 14a shows a decreasing trend from right to left (inner to outer galaxy) and an increasing scatter (more blue and red points towards the left) in the residual plot of Fig. 14b. We cannot identify a strong correlation between gas overdensities and stellar metallicity or residuals in either plot - possibly caused

by the low number density. In Figs. 14c and 14d, however, the radial gas metallicity gradient shows significant local variations, that is, a trend from left to right that is not very smooth. In particular, we find significant deviations of up to +0.15 dex in [Fe/H] behind the outer gas spiral (lower left of Fig. 14d) and –0.1 dex in [Fe/H] in front of the inner gas spiral (upper center of Fig. 14d) with a steep edge consistent with the gas spiral edge. We have identified the same patterns in both [Fe/H] and A(O) as both elements trace each other rather well in the simulation of **young stars and gas** (see App. ?? and its Fig. A1).

Tentatively, we even see a slight enhancement of A(O) at the trailing edge of the inner spiral arm (top of Fig. 14d). We convince ourselves of the step-like behaviour by selecting a small slit-like region of  $\varphi_{\text{Gal.}} \sim 0^\circ$  and  $-2 < Y_{\text{Gal.}} / \text{kpc} < -1$  and tracing the gas metallicity and gas density as a function of radius in Fig. 15. We indeed find steps and confirm that they coincide with the location of significant gas overdensities. These step-patterns have also been found by Grand et al. (2015) and Orr et al. (2023) in other simulations and observationally by Ho et al. (2017). While a simplified enrichment model by Ho et al. (2017) is able to explain oxygen abundance difference on the order of 0.08 dex as also seen in observations – similar to those in Fig. 15, we note that the used oxygen yields are notoriously uncertain (see Vincenzo et al. 2016, and references therein), and we thus focus more on the relative changes. In Fig. 15, we note an extended flat region just beyond  $R_{\text{Gal.}} > 10$  kpc, the best fitting  $R_{\text{break}}$  of an assumed piecewise linear fit.

Our analyses suggest that the correlation of void and overdensities with chemical enrichment of gas and young stars is more complicated and should better be followed up by tracing these structures over simulation look-back time in a dedicated follow-up analysis to unravel the physical mechanisms of star formation feedback cycles. This could also involve the tracing of star formation bursts and disk instabilities (Sánchez et al. 2014; Sánchez-Blázquez et al. 2014; Ho et al. 2015) as well as tracing how much self-enrichment as well as mixing and dilution takes place around the gas spirals (Ho et al. 2017). While we have confirmed that our results are mainly driven by large amounts of cold gas around 100–1000 K as well as hot ionized gas below 20 000 K, we note that smaller amounts of hot gas above 20 000 K shows similar trends, but larger

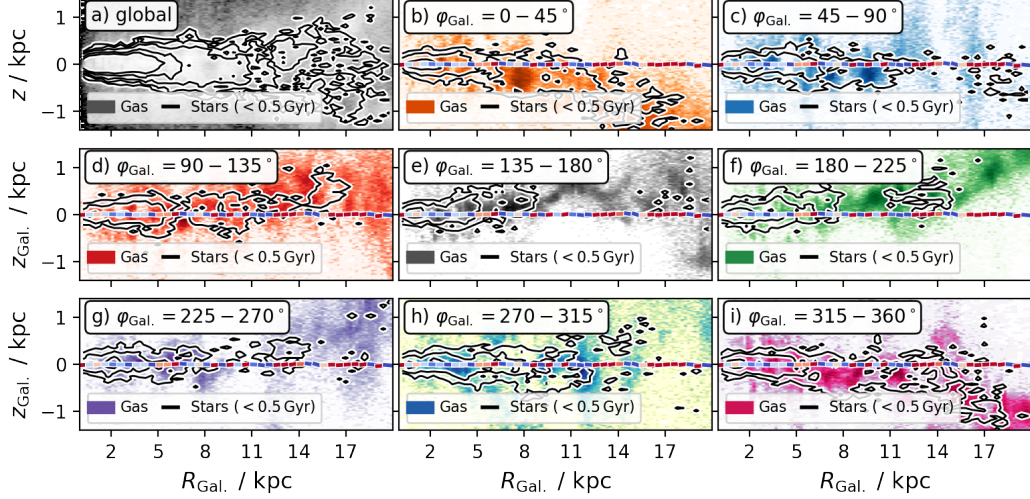


FIG. 12.— Tracing young stars and gas across galactocentric radii  $R_{\text{Gal.}}$ , and height  $z_{\text{Gal.}}$ , across the whole galaxy (panel a) and different azimuthal ranges/sectors (panels b-i). Small rectangles with cool-warm colors along the horizontal axis indicate the local gradient slopes as in Fig. 6.

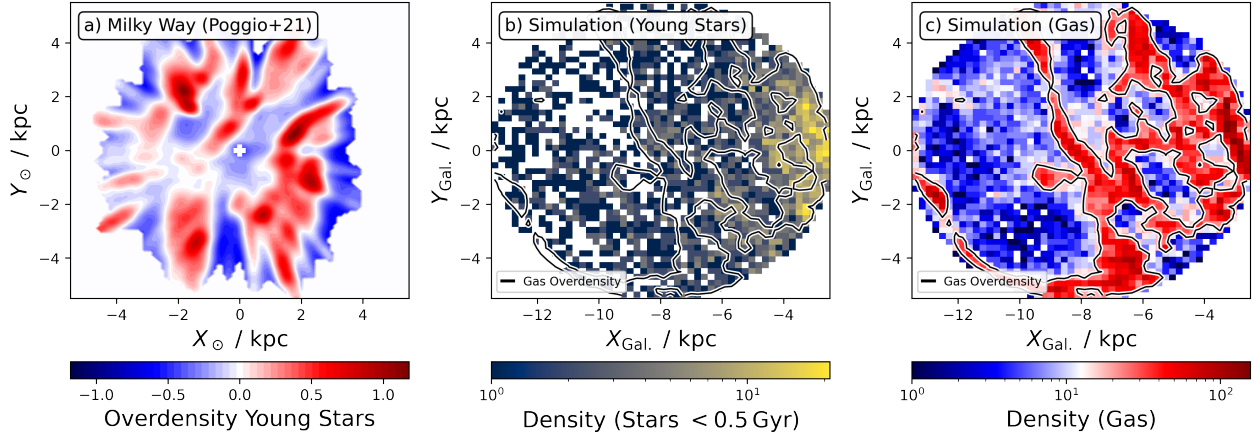


FIG. 13.— Comparison of the density distribution of young stars and gas in the Milky Way and the NIHAO Milky Way analogue simulation. Panel a) shows the measurements of the Solar vicinity within 5 kpc by Poggio et al. (2021). Panels b) and c) show young stars and gas NIHAO, respectively, for a selected region similar to panel a). Black and white contour lines in panel b) trace overdensities in the gas distribution of panel c).

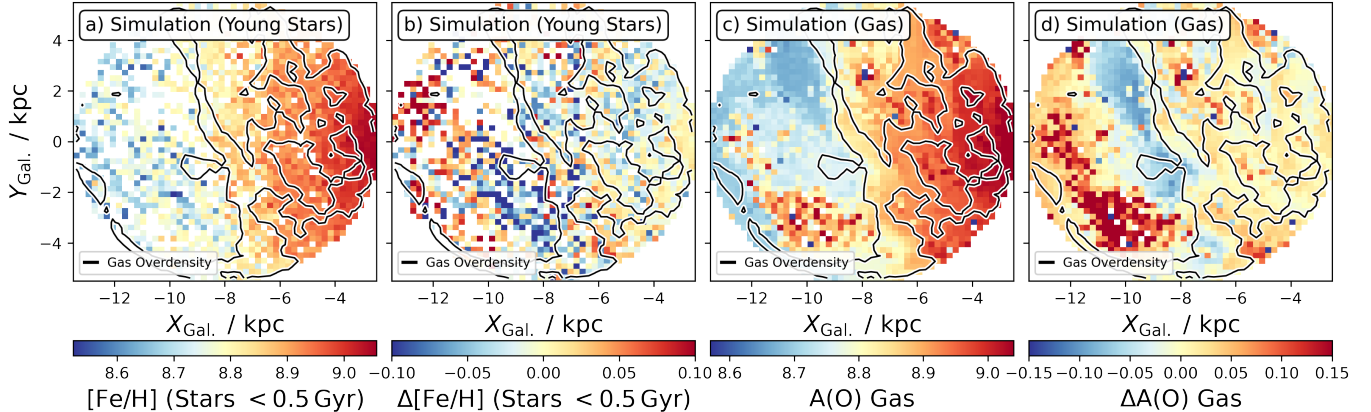


FIG. 14.— Comparison of density distribution of young stars and gas in the NIHAO-UHD Milky Way analogue simulation for the same regions as Figs. 13b and 13c. Panels a) and c) trace median young star Fe and gas O abundances, respectively. Panels b) and d) plot the metallicity residuals of stars and gas, respectively, when correcting with a radial metallicity gradient fit. Black and white contour lines in each panel trace overdensities in the gas distribution of Fig. 13c).

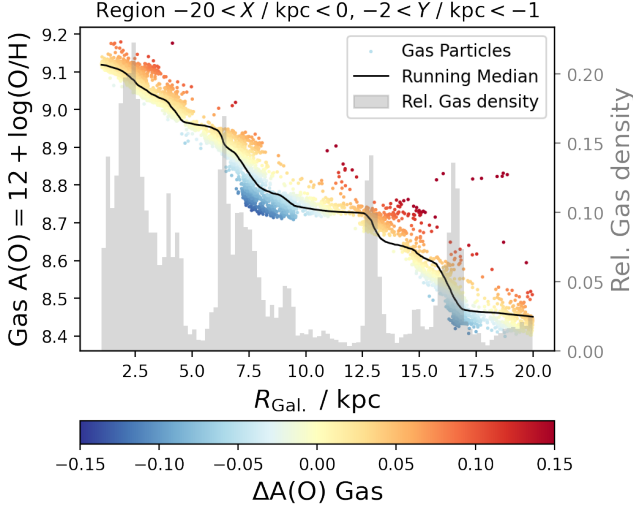


FIG. 15.— Radial gas metallicity gradient of a slit-like region ( $-2 < R_{\text{Gal.}} / \text{kpc} < -1$ ) from Fig. 14. The plot extends towards larger and smaller radii and shows the step-like distribution of individual gas particle metallicities colored by their deviation from a global fit. A running median along 1000 particles is shown as a black line. The gray histogram indicates the gas density along the radius with prominent overdensities coinciding with step edges.

**abundance spreads that could – once this gas cools down – translate into larger abundance spreads of later generations of stars (see App. B and its Fig. B1).** Rather than going back in simulation time, the present simulation data of a single snapshot in time already allows us to look back in terms of stellar lifetime – similar to Milky Way studies, as we discuss subsequently.

#### 5.4. The impact of time and age: mixing and migration

Although we have chosen a rather small stellar age window of 0.5 Gyr to trace the radial metallicity gradient without the expected significant impact of radial mixing and migration, we are testing and discussing this particular choice in this section in two ways. Firstly, we test the deviation of the radial metallicity gradient from the same global shape as well as the abundance spread across smaller age bins of 100 Myr between 0 – 1000 Myr in Fig. 16. Secondly, we trace the distribution of stellar metallicity across galactic radii for increasing age bins from 50 Myr up to the maximum stellar age of 13.8 Gyr in Fig. 17.

Our first test in Fig. 16 shows that the deviation from a global trend remains similar in functional form. We find that the spread of iron abundance does indeed scatter significantly, but the distributions stay within the same overall shape across the ten age bins. We note though, that the smallest age bin of 0 – 100 Myr shows the least abundance scatter.

This is consistent with the picture from our second test of increasing age ranges in Fig. 17. Here we find the first significant deviation from a tighter and already slightly quadratic relation for an age of 100 – 150 Myr in Fig. 17c - our previously identified Group 3. As expected from previous simulations and observations, we see an increase in the scatter as we include more and more older stars. We note a still similar albeit more scattered shape for stars below 4 Gyr in Fig. 17h, before we start to see a more metal-poor population of stars in the inner galaxy appear between 4 – 8 Gyr in Fig. 17i. These also begin to significantly impact the quadratic fit to the radial metallicity distribution, shown as a solid red line, in contrast to

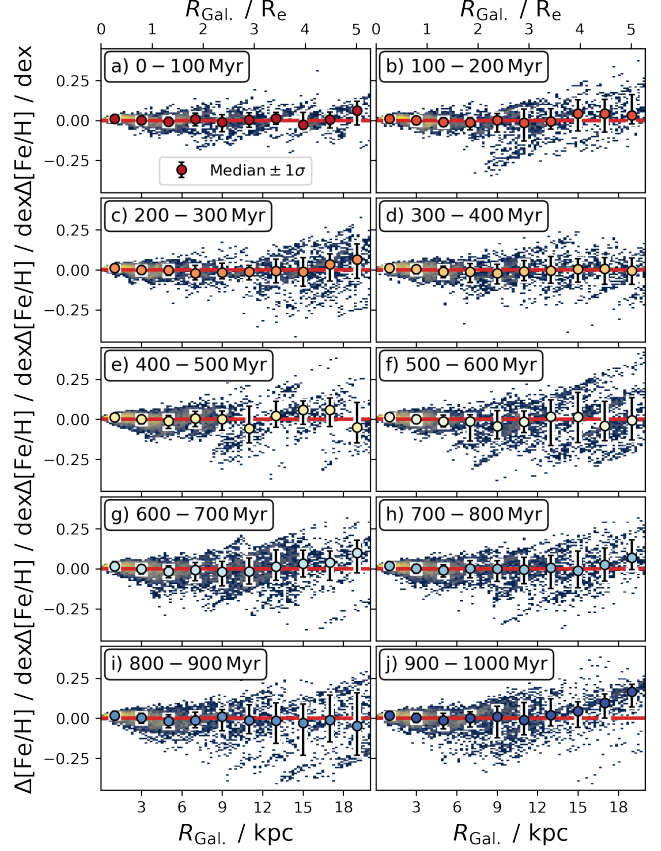


FIG. 16.— Stellar density distribution and spread of [Fe/H] across different galactocentric radii with respect to a global linear radial metallicity gradient across different age ranges. Panels a–j) show young stars and exhibit a rather similar trend, whereas the scatter increases significantly for stars above 0.5 Gyr in panels k) and l).

our reference fit, represented by a dashed red line. The significant amount of metal-poor stars in the inner galaxy then completely tilts the distribution when also including stars between 8 – 13.8 Gyr in Fig. 17j (see also Johnson et al. 2024). Similar to the Milky Way (Bland-Hawthorn & Gerhard 2016), these oldest stars are those of the relatively more metal-poor thick disk that are confined to the inner disk with a shorter scale length. **Including such old stars in metallicity gradient studies could significantly bias conclusions.**

While we cannot exclude radial migration playing a role for change of radius for the youngest stars of the simulation, since Frankel et al. (2018) predicted significant shifts even for ages below 0.5 Gyr (see their Fig. 10), the larger scatter for older stars is certainly suggesting a larger (re-)distribution of stars along the radial axis, as found in previous simulations (Minchev & Famaey 2010; Grand et al. 2015).

#### 5.5. Implications for Milky Way studies

Our analysis of the radial metallicity gradient in a simulated NIHAO-UHD galaxy offers several insights that are directly applicable to understanding the Milky Way’s gradient.

First, the nature of the gradient – whether it is linear or better described by more complex functional forms – remains a critical question. Previous studies, such as those by Lépine et al. (2011) and Donor et al. (2020), have suggested the potential for a break radius, possibly at the corotation radius or further out (Scarano & Lépine 2013), which could indicate

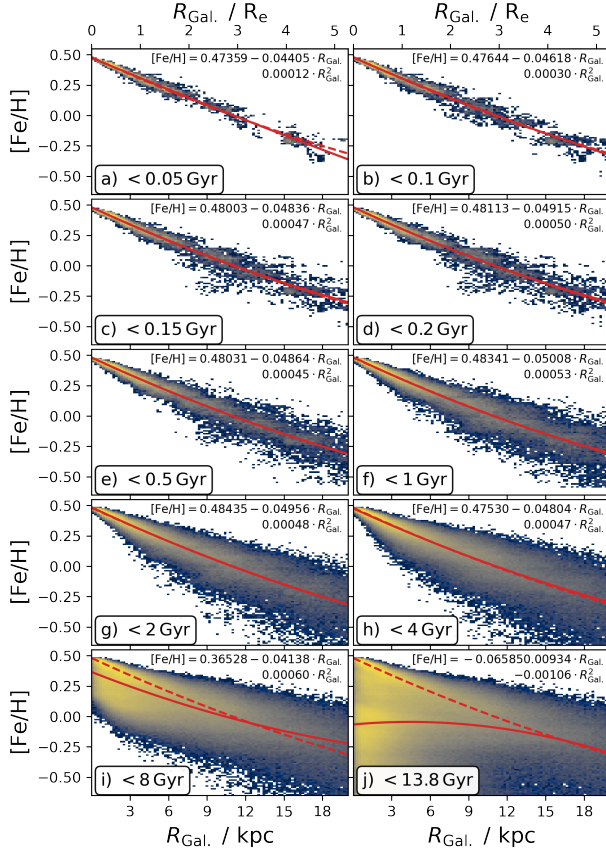


FIG. 17.— Radial metallicity gradients and quadratic fits for different maximum age ranges. The quadratic fit to stars below 0.5 Gyr is shown as a dashed red line for reference and the quadratic fit to each shown distribution is overlaid as a solid red line with the functional form given as inset text. At  $R_{\text{Gal.}} = 8.21 \text{ kpc}$ , spread increases from  $\sigma[\text{Fe}/\text{H}] = 0.05$  for youngest stars to 0.09 and 0.11 for stars below 4 and 8 Gyr, respectively.

two distinct linear regimes. In our analysis, we find evidence that the gradient is at least not purely linear, but could also be smoothly flattening. Applying a smooth quadratic function on observational data (Yong et al. 2012; Andrievsky et al. 2004; Genovali et al. 2014), might provide a better or at least consistent fit for the Milky Way data without the need for a break radius. However, even this may not fully capture the nuances observed in our simulations. Chemical evolution models propose a more sophisticated behaviour (e.g. Chiappini et al. 2001; Kubryk et al. 2015; Palla et al. 2024), reflecting varying influences of galactic processes at different radii. Understanding this structure in the simulated galaxy provides a framework for interpreting similar complexities in the Milky Way.

Given these complexities, it is also essential to consider how local sampling biases might affect our understanding of the Milky Way’s metallicity gradient. For instance, incomplete samples that omit low [Fe/H] clusters or stars could skew gradient estimates, as suggested by our comparisons in Figures 10a and 10b. Our results indicate that young clusters with lower (or higher) [Fe/H] than expected at a given radius could indicate the previous presence of a spiral arm (see our identified Groups in Figs. 8 and 9). Furthermore, we caution that localised effects – both intrinsic and in terms of selection function – could also mimic non-linear shapes and more spatial coverage is needed in the Milky Way. Our results also indicate that older clusters, which have been found more frequently at larger distances than young clusters – are likely

influenced by radial migration – and thus complicate the interpretation of these radial metallicity gradients (Magrini et al. 2009; Lépine et al. 2011).

Cosmological zoom-in simulations like NIHAO-UHD are approaching the resolution needed to examine regions analogous to the solar vicinity, though the star particle numbers and mass resolution remain a limiting factor. Nonetheless, we observe distinct patterns in the distribution of young stars and gas, including lower [Fe/H] and A(O) in the leading edges of gas overdensities and higher [Fe/H] and A(O) in the trailing edges, consistent with findings by Grand et al. (2016), Ho et al. (2017), and Kreckel et al. (2019). These trends suggest that local metallicity variations, driven by gas dynamics and bulk motions (see e.g. Orr et al. 2023), may also play a significant role in shaping the observed gradients in the Milky Way.

Additionally, our study hints at the potential for more nuanced variations in [Fe/H] across different regions of the galaxy. In particular, the gas shows a step-like behavior of A(O) and [Fe/H] changes around the edges of gas overdensities (Fig. 15), with significant deviations from the global gradient in specific regions. We have also found a larger stellar void around  $-12 < R_{\text{Gal.}} < -10 \text{ kpc}$ . Although further investigation is needed, these findings could have important implications for understanding localized star formation events and their impact on the overall metallicity distribution in the Milky Way (Sánchez et al. 2014; Sánchez-Blázquez et al. 2014; Ho et al. 2015). It will certainly be exciting to see how much more insights (Poggio et al. 2021; Hackshaw et al. 2024) we will get from the more extended data of future data releases of *Gaia* and spectroscopic surveys.

We cannot directly link spiral arms to bar resonances or bar-driven mixing in our simulation, because of a negligible bar strength in our galaxy<sup>3</sup> (but see Minchev & Famaey 2010; Di Matteo et al. 2013). However, the influence of a galactic bar on the spiral arms and, by extension, on the radial metallicity gradient, remains a possibility (see again Chen et al. 2023). Disk instabilities and warps might further complicate the interpretation of these gradients and progress will likely rely on the detailed disentangling of these effects from both cosmological simulations as well as idealised simulations and models (Minchev et al. 2013; Grand et al. 2015, 2016; Krumholz et al. 2018; Sharda et al. 2021; Bland-Hawthorn et al. 2024; Tepper-Garcia et al. 2024).

### 5.6. Implications for extragalactic studies

The insights gained from our analysis of the radial metallicity gradient in a simulated NIHAO-UHD galaxy extend beyond the Milky Way, offering valuable implications for the study of extragalactic systems.

One key observation is that deviations from a purely linear metallicity gradient, as seen in our Milky Way analogue, are common in other galaxies as well. When fitting a piecewise linear fit to our data, we found a break radius **at  $R_{\text{Gal.}} = 9.3 - 11.5 \text{ kpc}$** . Converted to effective radii  $R_e$  or radii  $R_{25}$  covering the  $25 \text{ mag arcsec}^{-2}$  isophote<sup>4</sup>, this corresponds **to  $R_{\text{break}} \sim 2.4 - 3.0 R_e \equiv 0.7 - 0.8 R_{25}$  for our simulation**. This would be consistent with the observational results by Sánchez et al. (2014) who found that breaks in metallicity gradients are common in both spiral and barred galaxies, with flattening of the abundance being evident beyond  $\sim 2 R_e$  (compare also

<sup>3</sup> The second Fourier component of the density distribution has an amplitude of only 0.02.

<sup>4</sup> We assume  $R_{25} = 3.6 R_e$  (Williams et al. 2009; Chen et al. 2023).

to Belfiore et al. 2017). Similar to our suggestion for Milky Way studies, we suggest to also test a smooth function, such as a quadratic one, on extragalactic observational data (e.g. Bresolin et al. 2012; Chen et al. 2023) to test the preference of a distinct break radius.

Although the focus of this research lies on the observable region of the Milky Way ( $R_{\text{Gal.}} < 20 \text{ kpc}$ ) and most other galaxies ( $R_{\text{Gal.}} < 2.5 R_e$ ), the finding of significant gradient changes in the outskirts of galaxies by Garcia et al. (2023), suggests to also test this region of our Milky Way analogue. Garcia et al. (2023, see their Fig. 4) found a metallicity floor in IllustrisTNG galaxies. When using their sample to identify a metallicity floor radius for a Milky Way mass galaxy with  $\log(M_\star/M_\odot) = 10.7$  (Bland-Hawthorn & Gerhard 2016) at redshift  $z \sim 0$ , we would expect to find it around  $25 - 30 \text{ kpc}$ . We therefore extend the analysed radius to  $R_{\text{Gal.}} \leq 100 \text{ kpc}$  (see Fig. 18) and indeed find a similar abundance floor of  $[\text{Fe}/\text{H}] \geq -0.64$  for young stars and  $A(\text{O}) \geq 8.12$  for the majority of gas (see Fig. 19 at a similar radius). We note that another galaxy without gas in this figure is a sufficiently large distance of  $92 \text{ kpc}$ , that is,  $(Y, Y, Z) = (-50, -75, 20) \text{ kpc}$ .

These lowest abundances remind us of two observational results. Firstly, the iron abundance floor is consistent with the lower end of the Milky Way thin - and coincidentally outer - disk of  $[\text{Fe}/\text{H}] \sim -0.7$  (Bensby et al. 2014; Buder et al. 2019). Secondly this oxygen abundance floor is consistent with the results by Grasha et al. (2022) from TYPHOON galaxy observations. Grasha et al. (2022) suggested this could be caused by changes in the ratio of supernovae II and AGB reflected by a changing ratio of nitrogen to oxygen abundance N/O which also flattens towards a lower plateau below metallicities of  $A(\text{O}) \sim 8.0$  (Nicholls et al. 2017). While we cannot follow this observation up with the present simulation, a similar simulation used by Buder et al. (2024b) has traced the relative contribution of both supernovae II and AGB and should be used to test this hypothesis in the future.

It is important to note that the chemical evolution model in the NIHAO-UHD simulations is constrained by the current, incomplete understanding of evolutionary pathways and yields (Buck et al. 2021), as well as by limitations in resolution and the imperfect physics inherent to cosmological zoom-in simulations (Buck 2020). Both could contribute to the identified differences in absolute and relative abundances across different scales - including a different scatter of abundances for example of the gas phase metallicity between NIHAO-UHD of up to  $0.1 \text{ dex}$  and the low scatter of  $0.03 - 0.05 \text{ dex}$  (and even lower on local scales) found by PHANGS-MUSE face-on observations (Kreckel et al. 2020). Extending our analysis to other simulations and further improving the resolution and physics of the simulations will be key in uniting the observational and theoretical insights into galactic chemical evolution on small and large scales. **Furthermore, it would be worth to further investigate the highly enriched gas (top-right of Fig. 19d). An initial investigation confirms that this gas is not only hotter, but also less dense than the typical gas in the plane and shows typically larger vertical velocities – consistent with outflows. Most excitingly, a significant fraction of this enhanced gas can be traced back to confined regions around  $x_{\text{Gal.}} \sim 30 \text{ kpc}$ ,  $-30 < y_{\text{Gal.}} / \text{kpc} < 15$  and  $z_{\text{Gal.}} \sim -5 \text{ kpc}$ , where several supernovae went off recently.**

Similar to more resolved and higher quality observations in the Milky Way, we also expect more, better, and diverse face-on and edge-on observations and analyses across a range of wavelengths by the PHANGS and GECKOS teams (Kreckel

et al. 2019, 2020; van de Sande et al. 2023) as well as the SDSS-V and MAGPI collaborations (Kollmeier et al. 2017; Foster et al. 2021; Mun et al. 2024; Chen et al. 2024a), among many other ongoing efforts.

## 6. CONCLUSIONS

To conclude our study, we first iterate the main take-away of our research in Section 6.1 before giving suggestions for future research in Section 6.2.

### 6.1. Take-Away

We have analysed the radial metallicity distribution of young stars and gas in the inner  $20 \text{ kpc}$  of a NIHAO-UHD Milky Way analogue (Fig. 1), finding a predominantly linear decrease (Figs. 2 and 3). Although our analysis of a single spiral galaxy simulation has limited applicability to the entire population of diverse spiral galaxies, it reveals several intriguing findings about the shape and local metallicity variations. The results we find in this work hold relevance for both the Milky Way and extragalactic research communities:

- Looking into the shape in detail, we find that **a linear function can reproduce the trend of the innermost  $R_{\text{gal}} < 10 \text{ kpc}$** , but piecewise linear and quadratic functions both perform better than a linear fit to the radial metallicity relation **out to  $R_{\text{gal}} < 20 \text{ kpc}$** . However, we see no significant preference between piecewise and quadratic functions based on our assessments (Fig. 4). While the specific slopes differ when fitting all points or binned data, they agree within the still rather small fitting uncertainties.
- We find that a piecewise linear function can effectively approximate a quadratic function across scales commonly applied in Milky Way and extragalactic studies. Local deviations become traceable below a spatial resolution of  $\Delta R_{\text{Gal.}} \leq 2 \text{ kpc}$  (Fig. 5).
- We see no strong correlations of deviations in the vertical direction across the whole simulation (Fig. 6). Such correlations could, however, be blurred by azimuthal effects, like the galactic warp, which needs to be disentangled in the azimuthal dimension.
- We find various deviations from the global trend in azimuthal direction, including gaps as well as isolated streaks of stars with similar  $[\text{Fe}/\text{H}]$  across  $\Delta R_{\text{Gal.}} = 2 - 6 \text{ kpc}$  (Fig. 7). These can introduce significant local over-/under-enhancement of up to  $\pm 0.2 \text{ dex}$  in  $[\text{Fe}/\text{H}]$  at a given radius.
- We find significant scatter across the radial metallicity distribution caused by streaks of stars born with similar  $[\text{Fe}/\text{H}]$  at similar times and similar but slightly extended regions of the galaxy (Figs. 8 and 9).
- Our results imply the need for more careful consideration of local intrinsic effects and selection effects on radial metallicity gradient and scatter studies in the Milky Way (Fig. 10).
- Expanding our work to the gas phase metallicity gradient (Fig. 11), we perform a preliminary comparison of observed and simulated young stars as well as simulated gas distribution and chemistry (Figs. 12 and 13), finding significant step-like changes in the gas chemistry at the leading and trailing edges of gas spirals, with lower and higher enhancement respectively (Figs. 14 and 15).

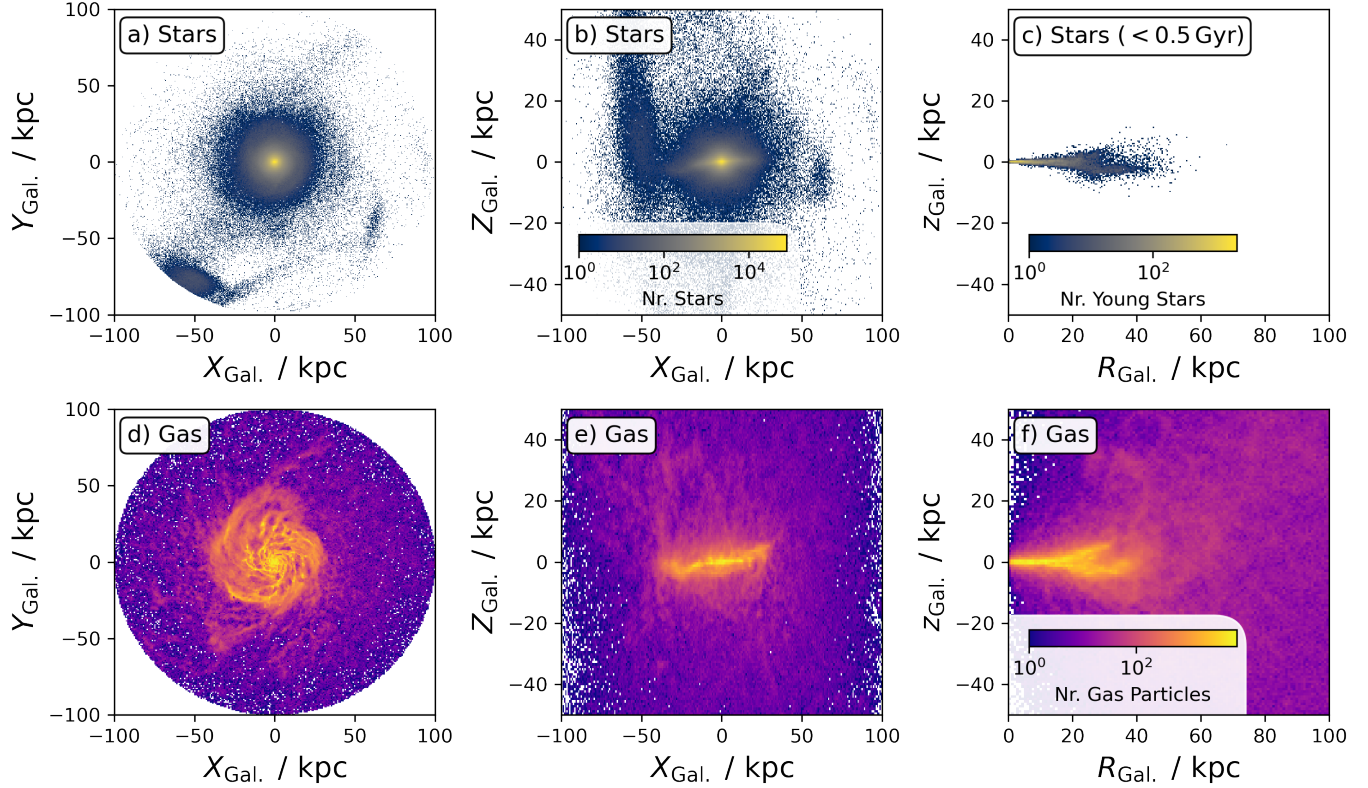


FIG. 18.— Same as Fig. 1, but for an extended  $R_{\text{Gal.}} \leq 100$  kpc and  $|z_{\text{Gal.}}| \leq 50$  kpc.

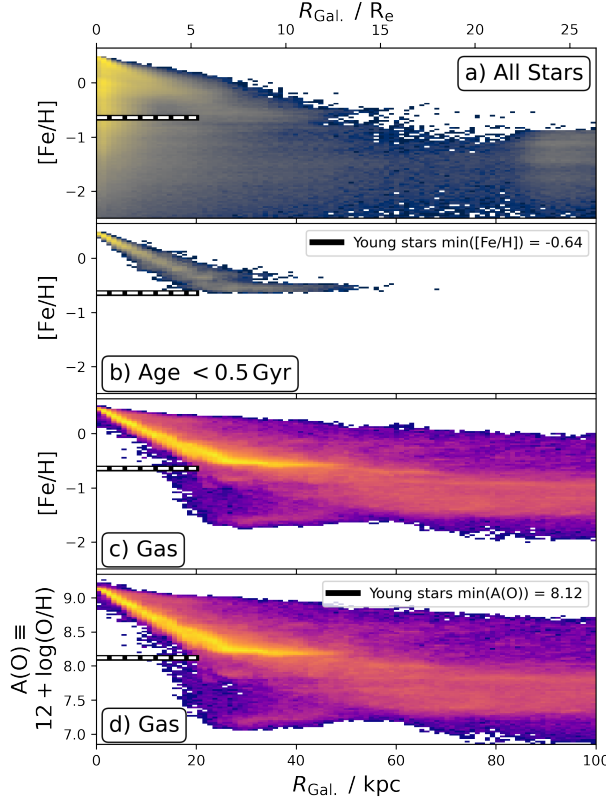


FIG. 19.— Radial metallicity functions for all stars (panel a), young stars (panel b), and gas (panels c and d for iron and oxygen as metallicity tracers) out to  $R_{\text{Gal.}} \leq 100$  kpc. Panels b and c are comparable to Figs. 3a and 11a for a smaller radial coverage.

- We have further identified that the abundance scatter, which increases towards larger radii, is as large as 0.1 dex and already present at the youngest ages of 100 Myr (Fig. 16). While not the focus of our analysis, we have also confirmed that the scatter significantly increases towards larger ages (Fig. 17).

- We have discussed the implications of our findings for studies of the Milky Way (Section 5.5) as well as external galaxies (Section 5.6). Here, we firstly suggest to explore the spread of abundances across different radii in more detail. Secondly, we suggest approaching the fitting of gradients in external galaxies in a more agnostic way to the shape. This will be particularly interesting when we can observe the outermost regions of galaxies, where simulations predict an abundance floor (Figs. 18 and 19).

## 6.2. Future Research

This study focused on a present-day snapshot of the NIHAO-UHD Milky Way analogue, akin to observations possible in our local Universe. Since the simulation traces particles and gas over time, a natural next step is to examine the temporal evolution and coherence of spatial and chemical over- and underdensities across different elements (see also Zhang et al. 2024). This would enable tracking abundance changes in the leading and trailing edges of spiral arms and follow their mixing and blurring over time. Establishing links to physical mechanisms and quantifying their roles requires further study. Upcoming datasets with broader coverage and improved stellar measurements (e.g. Barbillon et al. 2024) will also allow us to move beyond one-dimensional gradient analyses and better model local variations.

**While some elemental abundance trends are broadly consistent with observations (Buck et al. 2021; Buder et al. 2024b), uncertainties in enrichment sites, yields, and environments limit the predictive power of absolute abundances. Because of these limitations, and the simulation’s mass resolution constraints, we refrain from detailed comparisons to the actual Milky Way. Variations may also arise from different formation pathways, such as merger histories (Buck et al. 2023; Buder et al. 2024b). For example, our simulated galaxy exhibits a weak bar and a strong bulge ( $B/T = 0.48$  when selecting  $j_z/j_c < 0.5$  as bulge stars versus  $j_z/j_c > 0.7$  as disk stars via actions  $j$ ), similar to values found by Obreja et al. (2019) in a lower-resolution run of this simulation. These structural features align with results from Chen et al. (2023), who show that bar strength affects whether radial metallicity gradients change smoothly or feature distinct break radii. Motivated by the bar analysis of Tuntipong et al. (2024), future studies should investigate a larger sample of simulated galaxies to assess the role of bars in shaping gradient profiles. Expanding our work to other simulations, such as the VINTERGATAN suite (Renaud et al. 2024), and comparing to galaxies with varying mass, bar strength, formation history, or environment will help quantify their impact on metallicity gradients and disentangle the influence of different enrichment processes on galactic chemical evolution.**

## SOFTWARE

The research for this publication was coded in PYTHON (version 3.7.4) and included its packages ASTROPY (v. 3.2.2; Astropy Collaboration et al. 2013, 2018), IPYTHON (v. 7.8.0; Pérez & Granger 2007), MATPLOTLIB (v. 3.1.3; Hunter 2007), NUMPY (v. 1.17.2; Walt et al. 2011), PYNBODY (v. 1.1.0; Pontzen et al. 2013), SCIPY (v. 1.3.1; Virtanen et al. 2020),

SKLEARN (v. 1.5.1 Pedregosa et al. 2011) STATSMODELS (v. 0.14.2 Perktold et al. 2024) We further made use of TOPCAT (version 4.7; Taylor 2005);

## DATA AVAILABILITY

All code to reproduce the analysis and figures can be publicly accessed via [https://github.com/svenbuder/nihao\\_radial\\_metallicity\\_gradients](https://github.com/svenbuder/nihao_radial_metallicity_gradients). The used simulationsnapshot can be accessed as FITS file via [https://github.com/svenbuder/preparing\\_NIHAO](https://github.com/svenbuder/preparing_NIHAO). Original data, more snapshots and other galaxies can be found at [https://tobias-buck.de/#sim\\_data](https://tobias-buck.de/#sim_data). We encourage interested readers to get in contact with the authors for full data access and advice for use and cite Buck et al. (2020, 2021).

## ACKNOWLEDGMENTS

We acknowledge the traditional owners of the land on which the ANU stands, the Ngunnawal and Ngambri people. We pay our respects to elders past, and present and are proud to continue their tradition of surveying the night sky and its mysteries to better understand our Universe.

This work was supported by the Australian Research Council Centre of Excellence for All Sky Astrophysics in 3 Dimensions (ASTRO 3D), through project number CE170100013. SB and KG acknowledge support from the Australian Research Council under grant numbers DE240100150 and DE220100766, respectively. TB acknowledges funding from the Carl Zeiss Stiftung and support from the European Research Council under ERC-CoG grant CRAGSMAN-646955. We gratefully acknowledge the Gauss Centre for Supercomputing e.V. ([www.gauss-centre.eu](http://www.gauss-centre.eu)) for funding this project by providing computing time on the GCS Supercomputer SuperMUC at Leibniz Supercomputing Centre ([www.lrz.de](http://www.lrz.de)). Simulations were partially computed with High Performance Computing resources at New York University, Abu Dhabi.

## REFERENCES

- Agertz O., et al., 2021, *MNRAS*, **503**, 5826  
 Allende Prieto C., Beers T. C., Wilhelm R., Newberg H. J., Rockosi C. M., Yanny B., Lee Y. S., 2006, *ApJ*, **636**, 804  
 Anders F., et al., 2014, *A&A*, **564**, A115  
 Anders F., et al., 2017, *A&A*, **600**, A70  
 Andrievsky S. M., et al., 2002a, *A&A*, **381**, 32  
 Andrievsky S. M., Bersier D., Kovtyukh V. V., Luck R. E., Maciel W. J., Lépine J. R. D., Beletsky Y. V., 2002b, *A&A*, **384**, 140  
 Andrievsky S. M., Luck R. E., Martin P., Lépine J. R. D., 2004, *A&A*, **413**, 159  
 Astropy Collaboration et al., 2013, *A&A*, **558**, A33  
 Astropy Collaboration et al., 2018, *AJ*, **156**, 123  
 Barrillon M., Recio-Blanco A., Poggio E., Palicio P. A., Spitoni E., de Laverny P., Cescutti G., 2024, arXiv e-prints, p. arXiv:2411.10007  
 Belfiore F., et al., 2016, *MNRAS*, **461**, 3111  
 Belfiore F., et al., 2017, *MNRAS*, **469**, 151  
 Bellardini M. A., Wetzel A., Loebman S. R., Faucher-Giguère C.-A., Ma X., Feldmann R., 2021, *MNRAS*, **505**, 4586  
 Bellardini M. A., Wetzel A., Loebman S. R., Bailin J., 2022, *MNRAS*, **514**, 4270  
 Bensby T., Feltzing S., Oey M. S., 2014, *A&A*, **562**, A71  
 Bergemann M., et al., 2014, *A&A*, **565**, A89  
 Binney J., Tremaine S., 2008, Galactic Dynamics: Second Edition. Princeton University Press  
 Bird J. C., Kazantzidis S., Weinberg D. H., Guedes J., Callegari S., Mayer L., Madau P., 2013, *ApJ*, **773**, 43  
 Bland-Hawthorn J., Gerhard O., 2016, *ARA&A*, **54**, 529  
 Bland-Hawthorn J., Tepper-Garcia T., Agertz O., Federrath C., 2024, *ApJ*, **968**, 86  
 Boeche C., et al., 2013, *A&A*, **559**, A59  
 Bresolin F., Kennicutt R. C., Ryan-Weber E., 2012, *ApJ*, **750**, 122  
 Buck T., 2020, *MNRAS*, **491**, 5435  
 Buck T., Macciò A. V., Dutton A. A., Obreja A., Frings J., 2019, *MNRAS*, **483**, 1314  
 Buck T., Obreja A., Macciò A. V., Minchev I., Dutton A. A., Ostriker J. P., 2020, *MNRAS*, **491**, 3461  
 Buck T., Rybizki J., Buder S., Obreja A., Macciò A. V., Pfrommer C., Steinmetz M., Ness M., 2021, *MNRAS*, **508**, 3365  
 Buck T., Obreja A., Ratcliffe B., Lu Y., Minchev I., Macciò A. V., 2023, *MNRAS*, **523**, 1565  
 Buder S., et al., 2019, *A&A*, **624**, A19  
 Buder S., et al., 2024a, arXiv e-prints, p. arXiv:2409.19858  
 Buder S., Mijnarends L., Buck T., 2024b, *MNRAS*, **532**, 1010  
 Cantat-Gaudin T., Anders F., 2020, *A&A*, **633**, A99  
 Casamiquela L., et al., 2019, *MNRAS*, **490**, 1821  
 Chabrier G., 2003, *PASP*, **115**, 763  
 Chen Q.-H., Grasha K., Battisti A. J., Kewley L. J., Madore B. F., Seibert M., Rich J. A., Beaton R. L., 2023, *MNRAS*, **519**, 4801  
 Chen Q.-H., et al., 2024a, *MNRAS*, **527**, 2991  
 Chen Q.-H., et al., 2024b, *MNRAS*, **534**, 883  
 Chiappini C., 2002, *Ap&SS*, **281**, 253  
 Chiappini C., Matteucci F., Gratton R., 1997, *ApJ*, **477**, 765  
 Chiappini C., Matteucci F., Romano D., 2001, *ApJ*, **554**, 1044  
 Chieffi A., Limongi M., 2004, *ApJ*, **608**, 405  
 Chiosi C., 1980, *A&A*, **83**, 206  
 Cunha K., et al., 2016, *Astronomische Nachrichten*, **337**, 922  
 Di Matteo P., Haywood M., Combes F., Semelin B., Snaith O. N., 2013, *A&A*, **553**, A102  
 Donor J., et al., 2020, *AJ*, **159**, 199  
 Foster C., et al., 2021, *PASA*, **38**, e031  
 Frankel N., Rix H.-W., Ting Y.-S., Ness M., Hogg D. W., 2018, *ApJ*, **865**, 96  
 Frankel N., Sanders J., Ting Y.-S., Rix H.-W., 2020, *ApJ*, **896**, 15  
 Fraser-McKelvie A., et al., 2022, *MNRAS*, **510**, 320  
 Gaia Collaboration et al., 2016, *A&A*, **595**, A1  
 Garcia A. M., et al., 2023, *MNRAS*, **519**, 4716  
 Genovali K., et al., 2014, *A&A*, **566**, A37  
 Graf R. L., Wetzel A., Bellardini M. A., Bailin J., 2024, arXiv e-prints, p. arXiv:2402.15614  
 Grand R. J. J., Kawata D., Cropper M., 2015, *MNRAS*, **447**, 4018

- Grand R. J. J., et al., 2016, *MNRAS*, **460**, L94
- Grasha K., et al., 2022, *ApJ*, **929**, 118
- Hackshaw Z., Hawkins K., Filion C., Horta D., Laporte C. F. P., Carr C., Price-Whelan A. M., 2024, arXiv e-prints, p. arXiv:2405.18120
- Hayden M. R., et al., 2014, *AJ*, **147**, 116
- Hayden M. R., et al., 2015, *ApJ*, **808**, 132
- Hemler Z. S., et al., 2021, *MNRAS*, **506**, 3024
- Ho I. T., Kudritzki R.-P., Kewley L. J., Zahid H. J., Dopita M. A., Bresolin F., Rupke D. S. N., 2015, *MNRAS*, **448**, 2030
- Ho I. T., et al., 2017, *ApJ*, **846**, 39
- Hogg D. W., Eilers A.-C., Rix H.-W., 2019, *AJ*, **158**, 147
- Hunter J. D., 2007, *Comput Sci Eng*, **9**, 90
- Imig J., et al., 2023, *ApJ*, **954**, 124
- Janes K. A., 1979, *ApJS*, **39**, 135
- Johnson J. W., et al., 2024, arXiv e-prints, p. arXiv:2410.13256
- Karakas A. I., Lugaro M., 2016, *ApJ*, **825**, 26
- Kauffmann G., 1996, *MNRAS*, **281**, 475
- Khoperskov S., Sivkova E., Saburova A., Vasiliev E., Shustov B., Minchev I., Walcher C. J., 2023, *A&A*, **671**, A36
- Knollmann S. R., Knebe A., 2009, *ApJS*, **182**, 608
- Kollmeier J. A., et al., 2017, arXiv e-prints, p. arXiv:1711.03234
- Kreckel K., et al., 2019, *ApJ*, **887**, 80
- Kreckel K., et al., 2020, *MNRAS*, **499**, 193
- Krumholz M. R., Ting Y.-S., 2018, *MNRAS*, **475**, 2236
- Krumholz M. R., Burkhardt B., Forbes J. C., Crocker R. M., 2018, *MNRAS*, **477**, 2716
- Kubryk M., Prantzos N., Athanassoula E., 2015, *A&A*, **580**, A126
- Lacey C. G., Fall S. M., 1985, *ApJ*, **290**, 154
- Larson R. B., 1976, *MNRAS*, **176**, 31
- Lemasle B., François P., Bono G., Mottini M., Primas F., Romanelli M., 2007, *A&A*, **467**, 283
- Lemasle B., François P., Piersimoni A., Pedicelli S., Bono G., Laney C. D., Primas F., Romanelli M., 2008, *A&A*, **490**, 613
- Lemasle B., et al., 2013, *A&A*, **558**, A31
- Lemasle B., et al., 2022, *A&A*, **668**, A40
- Lépine J. R. D., et al., 2011, *MNRAS*, **417**, 698
- Li Z., et al., 2024, *MNRAS*, **528**, 7103
- Lilly S. J., Carollo C. M., Pipino A., Renzini A., Peng Y., 2013, *ApJ*, **772**, 119
- Lu Y., Buck T., Minchev I., Ness M. K., 2022, *MNRAS*, **515**, L34
- Ma X., Hopkins P. F., Feldmann R., Torrey P., Faucher-Giguère C.-A., Kereš D., 2017a, *MNRAS*, **466**, 4780
- Ma X., Hopkins P. F., Wetzel A. R., Kirby E. N., Anglés-Alcázar D., Faucher-Giguère C.-A., Kereš D., Quataert E., 2017b, *MNRAS*, **467**, 2430
- Magrini L., Sestito P., Randich S., Galli D., 2009, *A&A*, **494**, 95
- Magrini L., et al., 2017, *A&A*, **603**, A2
- Matteucci F., Recchi S., 2001, *ApJ*, **558**, 351
- Metha B., Trenti M., Chu T., 2021, *MNRAS*, **508**, 489
- Minchev I., Famaey B., 2010, *ApJ*, **722**, 112
- Minchev I., Chiappini C., Martig M., 2013, *A&A*, **558**, A9
- Minchev I., Chiappini C., Martig M., 2014, *A&A*, **572**, A92
- Minchev I., et al., 2018, *MNRAS*, **481**, 1645
- Moran S. M., et al., 2012, *ApJ*, **745**, 66
- Mun M., et al., 2024, *MNRAS*, **530**, 5072
- Myers N., et al., 2022, *AJ*, **164**, 85
- Nicholls D. C., Sutherland R. S., Dopita M. A., Kewley L. J., Groves B. A., 2017, *MNRAS*, **466**, 4403
- Obreja A., et al., 2019, *MNRAS*, **487**, 4424
- Obreja A., Buck T., Macciò A. V., 2022, *A&A*, **657**, A15
- Orr M. E., et al., 2023, *MNRAS*, **521**, 3708
- Osterbrock D. E., 1989, Astrophysics of gaseous nebulae and active galactic nuclei. University Science Books
- Palla M., Magrini L., Spitoni E., Matteucci F., Viscasillas Vázquez C., Franchini M., Molero M., Randich S., 2024, *A&A*, **690**, A334
- Pedregosa F., et al., 2011, *J Mach Learn Res*, **12**, 2825
- Pérez F., Granger B. E., 2007, *Comput Sci Eng*, **9**, 21
- Perktold J., et al., 2024, statsmodels/statsmodels: Release 0.14.2, doi:10.5281/zenodo.593847
- Pilkington K., et al., 2012, *A&A*, **540**, A56
- Pilyugin L. S., 2003, *A&A*, **397**, 109
- Pilyugin L. S., Tautvaišienė G., 2024, *A&A*, **682**, A41
- Pilyugin L. S., Grebel E. K., Zinchenko I. A., Nefedyev Y. A., Vilchez J. M., 2017, *A&A*, **608**, A127
- Planck Collaboration et al., 2014, *A&A*, **571**, A16
- Poggio E., et al., 2018, *MNRAS*, **481**, L21
- Poggio E., et al., 2021, *A&A*, **651**, A104
- Poggio E., et al., 2022, *A&A*, **666**, L4
- Pontzen A., Roškar R., Stinson G. S., Woods R., 2013, pynbody: Astrophysics Simulation Analysis for Python, Astrophysics Source Code Library, record ascl:1305.002
- Quirk W. J., Tinsley B. M., 1973, *ApJ*, **179**, 69
- Ratcliffe B. L., Ness M. K., Buck T., Johnston K. V., Sen B., Bernaldo e Silva L., Debattista V. P., 2022, *ApJ*, **924**, 60
- Ratcliffe B., et al., 2023, *MNRAS*, **525**, 2208
- Ratcliffe B., Khoperskov S., Minchev I., Lee N. D., Buck T., Marques L., Lu L., Steinmetz M., 2024, arXiv e-prints, p. arXiv:2410.17326
- Renaud F., Ratcliffe B., Minchev I., Haywood M., Di Matteo P., Agertz O., Romeo A. B., 2024, arXiv e-prints, p. arXiv:2409.10598
- Rolleston W. R. J., Smartt S. J., Dufton P. L., Ryans R. S. I., 2000, *A&A*, **363**, 537
- Rosales-Ortega F. F., Díaz A. I., Kennicutt R. C., Sánchez S. F., 2011, *MNRAS*, **415**, 2439
- Rybicki J., Just A., Rix H.-W., 2017, *A&A*, **605**, A59
- Sánchez-Blázquez P., et al., 2014, *A&A*, **570**, A6
- Sánchez-Menguiano L., et al., 2016, *A&A*, **587**, A70
- Sánchez S. F., et al., 2013, *A&A*, **554**, A58
- Sánchez S. F., et al., 2014, *A&A*, **563**, A49
- Scaramo S., Lépine J. R. D., 2013, *MNRAS*, **428**, 625
- Schöenrich R., Binney J., 2009, *MNRAS*, **396**, 203
- Searle L., 1971, *ApJ*, **168**, 327
- Seitenzahl I. R., et al., 2013, *MNRAS*, **429**, 1156
- Sharda P., Krumholz M. R., Wisnioski E., Forbes J. C., Federrath C., Acharyya A., 2021, *MNRAS*, **502**, 5935
- Shaver P. A., McGee R. X., Newton L. M., Danks A. C., Pottasch S. R., 1983, *MNRAS*, **204**, 53
- Spina L., et al., 2021, *MNRAS*, **503**, 3279
- Spitoni E., et al., 2023, *A&A*, **680**, A85
- Stanghellini L., Magrini L., Casasola V., 2015, *ApJ*, **812**, 39
- Stinson G., Seth A., Katz N., Wadsley J., Governato F., Quinn T., 2006, *MNRAS*, **373**, 1074
- Stinson G. S., Brook C., Macciò A. V., Wadsley J., Quinn T. R., Couchman H. M. P., 2013, *MNRAS*, **428**, 129
- Sun X., et al., 2024, arXiv e-prints, p. arXiv:2409.09290
- Taylor M. B., 2005, *ASPSC*, **347**, 29
- Tépper-García T., Bland-Hawthorn J., Vasiliev E., Agertz O., Teyssier R., Federrath C., 2024, arXiv e-prints, p. arXiv:2406.00342
- Tinsley B. M., 1980, *Fund. Cosmic Phys.*, **5**, 287
- Tissera P. B., Rosas-Guevara Y., Bower R. G., Crain R. A., del P Lagos C., Schaller M., Schaye J., Theuns T., 2019, *MNRAS*, **482**, 2208
- Tuntipong S., et al., 2024, arXiv e-prints, p. arXiv:2408.12223
- Twarog B. A., 1980, *ApJ*, **242**, 242
- Twarog B. A., Ashman K. M., Anthony-Twarog B. J., 1997, *AJ*, **114**, 2556
- Vickers J. J., Shen J., Li Z.-Y., 2021, *ApJ*, **922**, 189
- Vilchez J. M., Esteban C., 1996, *MNRAS*, **280**, 720
- Vincenzo F., Matteucci F., Belfiore F., Maiolino R., 2016, *MNRAS*, **455**, 4183
- Virtanen P., et al., 2020, *Nature Methods*, **17**, 261
- Wadsley J. W., Keller B. W., Quinn T. R., 2017, *MNRAS*, **471**, 2357
- Walt S. v. d., Colbert S. C., Varoquaux G., 2011, *Comput Sci Eng*, **13**, 22
- Wang L., Dutton A. A., Stinson G. S., Macciò A. V., Penzo C., Kang X., Keller B. W., Wadsley J., 2015, *MNRAS*, **454**, 83
- Willett E., et al., 2023, *MNRAS*, **526**, 2141
- Williams M. J., Bureau M., Cappellari M., 2009, *MNRAS*, **400**, 1665
- Wyse R. F. G., Silk J., 1989, *ApJ*, **339**, 700
- Yong D., Carney B. W., Friel E. D., 2012, *AJ*, **144**, 95
- Zari E., Hashemi H., Brown A. G. A., Jardine K., de Zeeuw P. T., 2018, *A&A*, **620**, A172
- Zari E., Rix H. W., Frankel N., Xiang M., Poggio E., Drimmel R., Tkachenko A., 2021, *A&A*, **650**, A112
- Zaritsky D., Kennicutt Robert C. J., Huchra J. P., 1994, *ApJ*, **420**, 87
- Zhang C., Li Z., Hu Z., Krumholz M. R., 2024, arXiv e-prints, p. arXiv:2411.01518
- van de Sande J., Fraser-McKelvie A., Fisher D. B., Martig M., Hayden M. R., the GECKOS Survey collaboration 2023, arXiv e-prints, p. arXiv:2306.00059

## APPENDIX

### A. GAS PHASE OXYGEN AND IRON ABUNDANCES

Fig. A1 demonstrates the tight correlation of gas phase iron and oxygen abundance and how to approximate them linearly. While observations typically show higher [O/H] at lower [Fe/H] (e.g. Buder et al. 2024a), we attribute the rather flat relation to the dominating contribution from core-collapse supernovae of massive stars to both O and Fe, a similar level of contribution of asymptotic giant branch stars to O and Fe as well as a lower amount of delayed contributions from supernovae type Ia across time in the simulation (see also Buck et al. 2021).

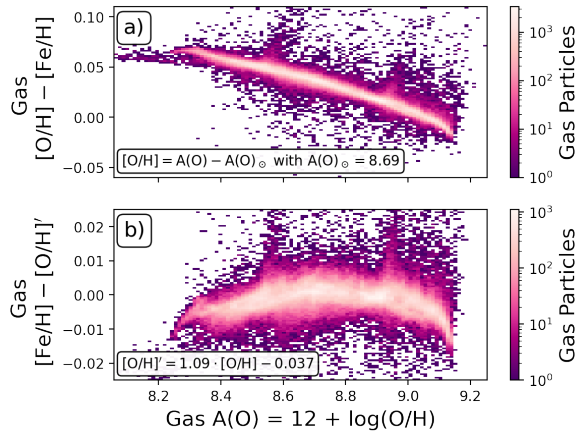


FIG. A1.— Comparison of gas abundances for oxygen and iron. Shown are absolute oxygen abundances  $A(O)$  and the comparison of relative iron and oxygen abundances  $[Fe/H] - [O/H]$ . The top panel shows values at face values, whereas the bottom panel shows the comparison for a linear approximation of  $[Fe/H]$  from  $[O/H]$ .

### B. SPATIAL DISTRIBUTION AND OXYGEN ABUNDANCES FOR DIFFERENT GAS TEMPERATURES

To assess the robustness of our analysis of the gas phase oxygen abundances, for example if we would mainly trace abundances through ionised gas like that in HII regions, we examine the temperature distribution of gas within  $R_{\text{Gal.}} < 20 \text{ kpc}$  in Fig. B1. In Fig. B1a, see that the gas temperatures of our simulation includes a significant amount of cool and warm neutral gas at the lower temperature end as well as a significant amount of ionised material at the higher end. The distribution peaks around  $10^{4.2} \text{ K} \approx 16000 \text{ K}$  – within the region of  $10000^{+10000}_{-5000} \text{ K}$  tabulated by Osterbrock (1989) for HII regions. We thus divide the gas in different temperature bins of  $\log_{10}(T_{\text{Gas}} / \text{K})$  within 2-3 (cold gas, shown in blue), 3-3.85 (warm gas in

green), 3.85-4.05 (warm ionised gas in orange), 4.05-4.3 (hot ionised gas in red), and above 4.3 (hottest ionised gas in purple).

We show the spatial distribution of the gas with these different temperatures in the left columns of Fig. B1. As expected, we see the cold and warm neutral medium quite tightly constrained on narrow spiral arms. While the warm ionised medium is still following the same pattern (Fig. B1j), we note that it is more spatially extended around the arms. The hot ionised medium (Fig. B1m) is well distributed across the plane. The hottest gas (Fig. B1p) is then again constrained to entirely different regions, including small and localised patches as well as the innermost radii of the galaxy. Most important for HII observations would be Figs. B1j and B1m, which show quite a significant change in how much gas is distributed away from the spiral arms themselves. This would be especially important, if we see a significantly different behaviour of the gas phase metallicity of oxygen abundance between these two phases.

We thus use the same temperature bins and plot the radial oxygen abundance gradient in the middle column of Fig. B1. Here, we firstly note that the warm neutral, and warm ionised medium follow a similar pattern and are also closely aligned with the abundances cold neutral medium (which seems slightly more constrained to the inner part of the galaxy). The most drastic change is again seen when going above temperatures of 10 000 K between Figs. B1k and B1n. Here, the logarithmic color map suggests a stronger increase of scatter. The median abundances agree, however, well with the trend of the cooler gas. This is not the case for the hottest ionised medium (Fig. B1q), which shows increased abundances with respect to the cooler gas. To confirm this qualitative impression, we have calculated the distribution (16th, 50th, and 84th percentiles) of gas within different temperature and radial bins.

The oxygen abundance distribution remains consistent between  $T_{\text{Gas}} = 10^2 - 10^{4.2} \text{ K}$ , with only a mild increase in spread from 0.03 to 0.05 dex. Above  $T_{\text{Gas}} = 20000 \text{ K}$ , the scatter increases more significantly (to 0.08-0.11 dex), but the median trends remain comparable to those at lower temperatures. Therefore, assuming HII regions primarily trace gas with  $T_{\text{Gas}} < 20000 \text{ K}$  we confirm that the observed oxygen abundance patterns and their scatter are consistent across these phases. The use of oxygen abundances for all gas particles as a proxy for those of HII regions thus appears justified in this regime, but future studies should take a closer look at the more nuanced difference in spatial distribution and abundances for the different gas temperatures.

This paper was built using the Open Journal of Astrophysics L<sup>A</sup>T<sub>E</sub>X template. The OJA is a journal which provides fast and easy peer review for new papers in the astro-ph section of the arXiv, making the reviewing process simpler for authors and referees alike. Learn more at <http://astro.theoj.org>.

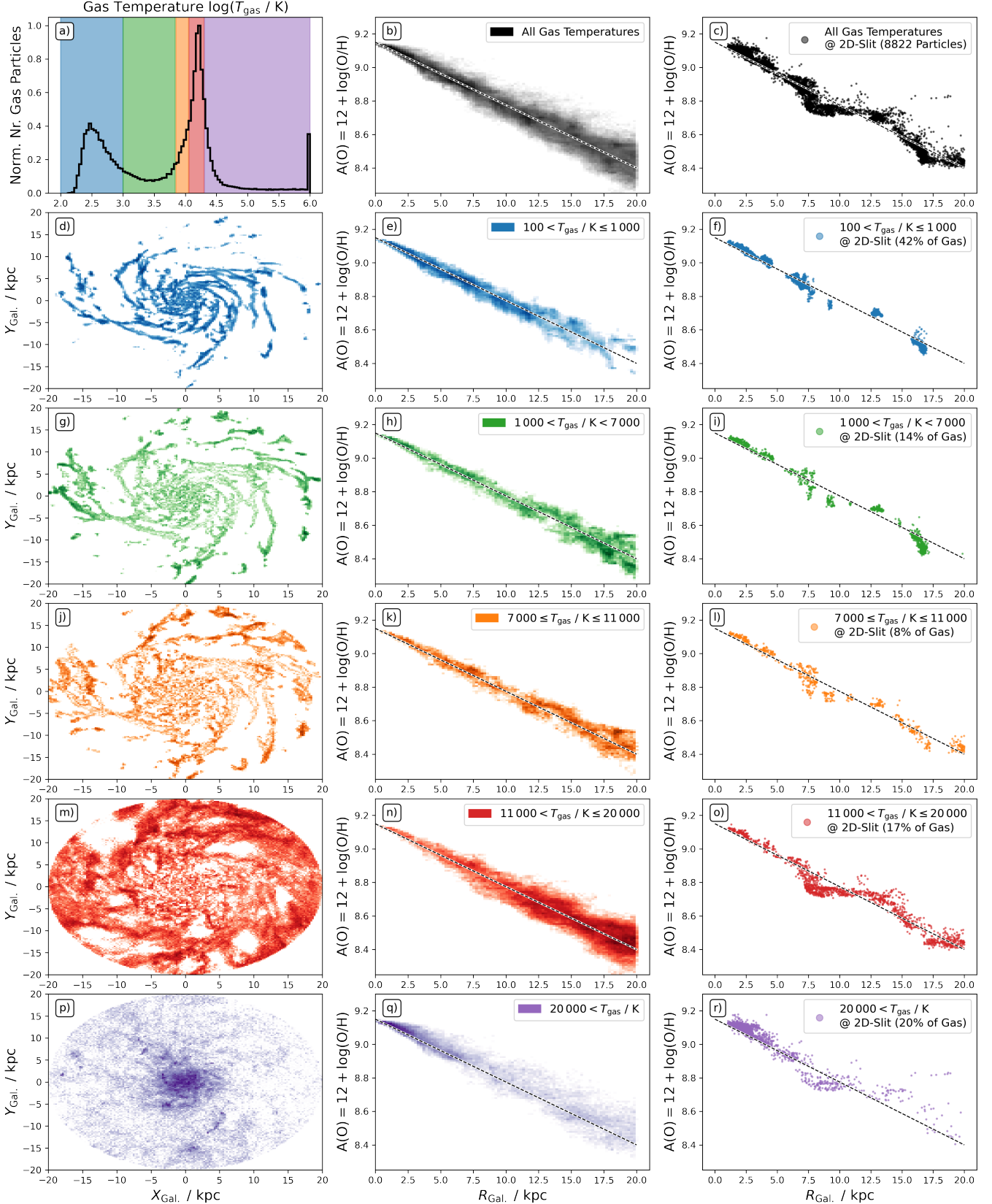


**Fig. B1.— Spatial distribution and oxygen abundances of gas with different gas temperatures.** Panel a) shows the gas temperature distribution with different groups (cold and warm neutral medium as well as ionized gas with different temperatures) highlighted. The histogram is saturated at  $10^5$  K to better visualize the temperature distribution. The left columns show the spatial distribution of these different groups. The other columns show the radial distribution of oxygen abundances for the full gas disk (middle columns) as well as the same 2-dimensional slit used for Fig. 15 (right columns). We show the same dashed line in the  $R_{\text{Gal}}\text{-}A(\text{O})$  panels to guide the eye.